Modelling the Nonthermal Emission of the Pulsar Wind Nebula MSH 15–52

Bachelorarbeit aus der Physik

vorgelegt von

Sebastian Meßlinger

Tag der Abgabe: 1. Juli 2013

Erlangen Centre for Astroparticle Physics
Physikalisches Institut
Friedrich-Alexander-Universität
Erlangen-Nürnberg

1. Gutachterin: Prof. Dr. Gisela Anton
2. Gutachterin: Dr. Ira Jung

This page is unintentionally left blank.

Abstract

Neutron stars are the super dense and highly magnetized remnants of stars undergoing a core collapse supernova. The enormous field strengths combined with the loss of rotational energy power a particle wind that can form a surrounding nebula. In this thesis, the nonthermal emission of the pulsar wind nebula (PWN) MSH 15–5*2* is modeled assuming a leptonic particle wind. Based on a spatially resolved X-ray analysis with `XMM-Newton` using annulus shaped extraction regions, a spherically symmetric model is used to estimate the physical parameters of the PWN. From this, the energy distribution of the leptons and the resulting expected flux from synchrotron and inverse Compton radiation are obtained. The latter is compared to observations in the very-high-energy (VHE) γ-ray domain with `H.E.S.S.` Two main scenarios reasonably compatible with the VHE data emerged during the modeling. Yet due to somewhat problematic X-ray data extraction and comparison as well as the apparently unconstrained preferences of the model in one parameter, it is unclear to what extend the results of the modeling have predictive value.

Zusammenfassung

Neutronensterne sind die superdichten und stark magnetisierten Überreste von Kernkollapssupernovae. Die gigantischen Feldstärken treiben zusammen mit dem Verlust von Rotationsenergie einen Teilchenwind an, der den umgebenden Nebel erhellen kann. In dieser Bachelorarbeit wird die nicht-thermische Strahlung des Pulsarwindnebels MSH 15–5*2* unter der Annahme eines leptonischen Teilchenwindes untersucht. Aufbauend auf ringförmigen Extraktionsregionen einer Röntgenanalyse mit `XMM-Newton` wird der Pulsarwindnebel mittels eines sphärisch symmetrischen Modells simuliert um die physikalischen Parameter des Nebels abzuschätzen. Aus der damit verbundenen Energieverteilung der Leptonen wird dann der erwartete Fluss von Synchrotron- und Invers-Compton Strahlung berechnet. Die Invers-Compton Strahlung wird mit Beobachtungen der `H.E.S.S.`-Teleskope im Very-High-Energy(VHE)-Gamma-Bereich verglichen. Während der Modellierung ergaben sich zwei verschiedene Szenarien, die mit den VHE-Gamma-Daten verträglich waren. Allerdings ist fraglich, wie viel physikalische Vorhersagen mit diesen Resultaten möglich sind, da das Vergleichskriterium stark von einem Parameter abhängt und Zweifel an der Zuverlässigkeit der Röntgendaten bestehen.

Contents

List of Figures

List of Tables

1. Introduction

While supernovae and accreting black holes are the superstars of astrophysics due to their gigantic energy output and mind bending properties, pulsars and especially their pulsar wind nebulae (PWNe) are seldom discussed in popular science. Still well in the realm of high energy astrophysics, these objects feature complex interactions between electromagnetic fields, shock waves and particles up to the highest energies. They therefore offer a rich environment for testing and developing theories from the fields of plasma and astroparticle physics.

PWNe exhibit a large spectrum of individual properties and it is therefore difficult to make generalized statements, especially considering the fact that all those properties are only accessible to us via passive observation. We only begin to understand some aspects of these systems, yet it is remarkable that we are already able to deduce so much about physical processes that are to date unthinkable to replicate on Earth, both in terms of energy and scale. Especially in cases like this, the basic method of physics, simplifying a system until it can be described in consistent fashion, has come a long way: It is a herculean task to describe such a complex system in a purely analytical fashion. Yet numerical models provide a method for testing approximations and a way of answering problems in individual cases that can not be solved in the general case.

This thesis will examine a rather young and energetic PWN, MSH 15–52, and try to improve constraints on the parameters compared with previous analyses. This is done by applying a time independent model based on a new X-ray analysis and comparing the output to γ-ray observations.

1.1. Pulsar Wind Nebulae

After a star with mass between $9\,M_\odot$ and $\sim 25\,M_\odot$ undergoes a core-collapse-supernova, a neutron star may get left behind [Heger et al., 2003]. Due to the conservation of angular momentum, these objects spin up rapidly, as a mass of $1.4\,M_\odot$ to $3.2\,M_\odot$ is compressed into a sphere with a radius of about 10 km, resulting in rotation periods as short as single digit milliseconds. Likewise the magnetic field of the star is conserved during collapse, the field compresses and the magnetic field strength increases to the order of $10^5 - 10^9$ T.

Such objects were first discovered in the radio band as rapidly and extremely regularly pulsing sources and therefore the term *pulsar* was coined. These pulses are caused by the dipole radiation emitted by the compressed magnetic field if its poles are not aligned with the rotational axis. The energy lost via radiation causes the period of the pulsar P to increase over time.[1] It is usually assumed that the observed spin down of pulsars is largely due to this mechanism [Gaensler and Slane, 2006], hence the term *spin-down luminosity* $L(t)$. This loss of rotational energy can be expressed as

$$L(t) = -\frac{\mathrm{d}E}{\mathrm{d}t} = 4\pi^2 I \frac{\dot{P}}{P^3} \quad , \tag{1.1}$$

I denotes the moment of inertia of the neutron star and $\dot{P} = \mathrm{d}P/\mathrm{d}t$ is the period derivative. For the initial period of the neutron star P_0 and the period at the current time P, the age of the pulsar is given by

[1] There are some pulsars though, that actually speed up by accreting material off of a companion star.

$$\tau = \frac{P}{(n-1)\dot{P}}\left(1-\left(\frac{P}{P_0}\right)^{n-1}\right) \quad . \tag{1.2}$$

Often the *characteristic age* is used, which is obtained from the true age by setting the *braking index* $n = 3$ and assuming $P \gg P_0$:

$$\tau_c = \frac{P}{2\dot{P}} \quad . \tag{1.3}$$

The rapidly rotating magnetic field also induces an electric field at the surface of the pulsar. The electrostatic potential is of quadrupolar form (Ω is the angular frequency and R the radius of the neutron star):

$$\phi = -\frac{B_0 \Omega R^5}{6r^3}\left(3\cos^2\theta - 1\right) \quad . \tag{1.4}$$

As the material of the neutron star is superconducting, this results in a charge distribution with respect to θ, the latitude on the neutron star. Negative charges dominate close to the poles and positive charges at the equator. Differentiation in radial direction of eq. (1.4) yields an electric field in the order of

$$|\mathbf{E}| \approx \Omega R B_0 \approx \frac{6 \cdot 10^{12}\,\mathrm{V/m}}{P} \tag{1.5}$$

[Longair, 2011].

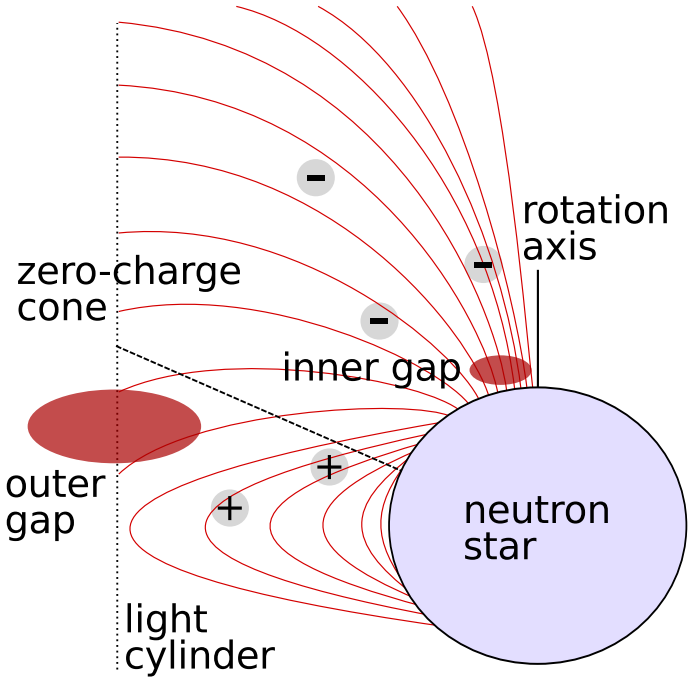

Figure 1: Schematic of the magnetosphere surrounding the pulsar. The outer acceleration gap is located at the boundary between closed and open field lines at the light cylinder. The magnetic field corotates with the pulsar, the “wind-up” of the field lines at the poles is not shown.

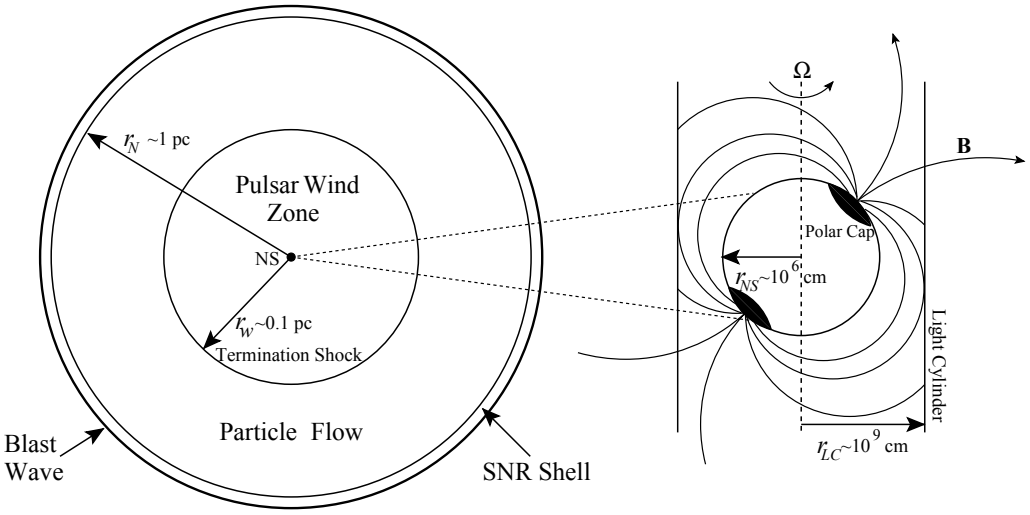

Figure 2: Schematic representation of a pulsar, its wind and the surrounding pulsar wind nebula. The size scale is logarithmic; figure taken from Slane [2005]

Electrons, in contrast to protons, are not held in place by nuclear forces, and hence can overcome the work function and gravitational attraction and are ripped out of the outer layer of the neutron star by the electric field. The escaping particles create a plasma surrounding the neutron star in which the field configuration and the charge separation is maintained[2]. The energy required for photons to initiate pair production is ~ 1 MeV. The curvature radiation the leptons of the plasma radiate on their trajectories along the magnetic field lines is sufficient to create photons with energies high enough to overcome this limit. Those photons interact with the magnetic field to produce further leptons, which in turn can create photons. This way, a pair-production cascade is initiated.

In the zero-charge cone (see Figure 1) close to the polar cap of the pulsar, this cascade results in *sparks* where newly created charges short out the separation and create perturbations in the electro-magnetic field. Though this process is not yet well understood, it is believed that these zones are the main source of particle emission of the pulsar, hence the name *inner acceleration gap*. Similarly, close to the light cylinder of the pulsar, the leptons are no longer confined to the co-rotating magnetic field and the separation collapses in the *outer acceleration gap* [Longair, 2011]. The ratio with which these mechanisms contribute is still unknown.

These highly relativistic particles stream outwards and form the *pulsar wind*. The particles are propagating along the field lines of the magnetic field which is in turn frozen into the plasma flow. Thus wind is described as “cold”, as the motion in the rest system of the particles relative to each other is comparatively small.

The pulsar wind expands into the more slowly expanding supernova ejecta, and a standing shock is formed, where the internal pressure of the pulsar wind equals the pressure in the surrounding medium. In this *termination shock*, the particles are scattered and the cold laminar flow becomes thermalized [Gaensler and Slane, 2006]. Also leptons are accelerated to very high energies, e.g. via the mechanism of Fermi-Acceleration, which is described in section 1.3.1.

[2]Some models also predict ions to escape from the equator regions to maintain charge neutrality in the plasma.

Downstream of the shock, the now hot leptons flow into the supernova remnant (SNR) to form the *pulsar wind nebula*, where they lose energy due to synchrotron radiation. The whole system is depicted in Figure 2.

Though the mechanism of acceleration close to the pulsar requires a large portion of the energy to be radiated as Poynting flux, the observed luminosity in synchrotron radiation requires a much larger fraction of particle flux close to the termination shock (see section 1.3.3 and section 3.1.1 for further details). The exact mechanism of this transition is still being discussed e.g in Spitkovsky and Arons [2002].

1.1.1. Evolution of Pulsar Wind Nebulae

In the initial phase of its life, the pulsar and its wind are surrounded by slowly expanding ejecta from the supernova explosion. The energy output is almost constant over a time of

$$\tau_0 = \frac{P_0}{(n-1)\dot{P}_0} \quad , \tag{1.6}$$

with a braking index n, often assumed to be $n = 3$. After that time the luminosity drops according to $L(t) \propto t^{(-n-1)/n-1}$.

This continuous energy injection causes significant overpressure compared to the surrounding medium and the PWN expands supersonically into the ejecta, forming a shock wave. In this state of the system, the spatial velocity of the pulsar stemming from asymmetries in the initial explosion (typically in the order of hundreds of km/s) is slow compared to the speed of sound in the surrounding medium ($v = c/\sqrt{3}$), the PWN stays centered on the pulsar. As the PWN expands, more and more particles lose their energy due to synchrotron radiation. This happens faster for higher energies, thus the PWN appears larger at lower wavelengths [Slane et al., 2000].

Typically a few thousand years after the supernova explosion, the SNR shell reaches the Sedov phase and spawns a reverse shock that travels inwards, eventually colliding with the still expanding PWN and compressing it. By then, the pulsar has typically been displaced from the center of the PWN. The collision initiates a quite complex interaction which causes the size of the PWN to oscillate a few times and may result in major deformation or complete displacement of the pulsar from the PWN.

After the plasma settles, the pulsar can once again power an expanding PWN, but contrary to the situation after the detonation, it now expands into hot, shocked ejecta and does not accelerate to supersonic speeds. Eventually the pulsar leaves the SNR and, when the speed of sound in the thinner outer regions of the SNR drops below the spatial velocity and begins to form a *bow shock PWN* [Gaensler and Slane, 2006].

1.1.2. MSH 15–52

The PWN MSH 15–52 has been the subject of extensive studies in the past. It is located in the galactic plane at a distance of (5.2 ± 1.4) kpc from Earth [Gaensler, Brazier, et al., 1999]. In the X-ray band the PWN extends over more than 300" [Schöck et al., 2010]. It is associated with the pulsar PSR 1509–58 and the SNR 320.4–1.2. In Figure 3 an overview of the PWN, taken

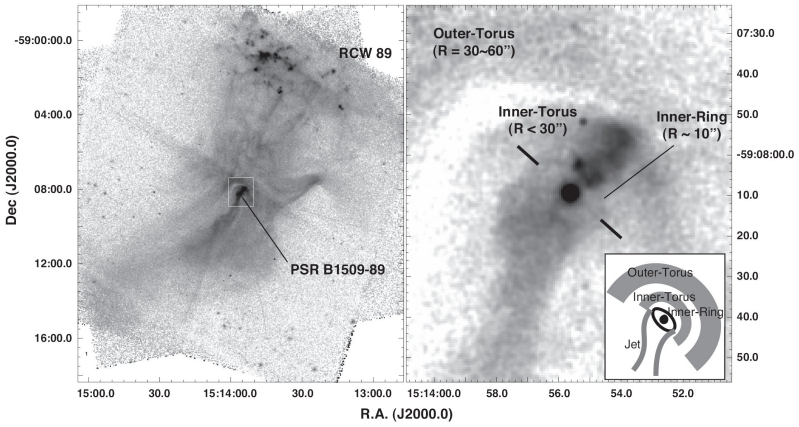

Figure 3: Overview X-ray image of MSH 15–5*2* with 190 ks exposure time taken by Chandra. The image was smoothed with a Gaussian of $\sigma = 2$", for the close-up image on the right, depicting the pulsar vicinity smoothing with $\sigma = 0.5$". The inner panel in the lower right-hand corner schematically describes the remarkable structures as described by Yatsu et al. [2009]. The inner ring at 10" is a candidate for the position of the termination shock. The pulsar's label should be PSR B1509-58 instead of PSR B1509-89

with the Chandra observatory, is depicted. *MSH* denotes the radio catalog compiled by Mills, Slee and Hill, as the PWN was first discovered as an extended radio source by a survey carried out by Mills et al. [1961], even before the discovery of the associated pulsar. Manchester et al. [1982] later discovered a pulsing radio source inside the nebula with the help of the *Einstein* X-ray observatory. The pulsar's surface magnetic field is estimated at $B = 1.5 \cdot 10^{13}$ G [Kaspi et al., 1994]. Manchester et al. [1982] determined a period of 150 ms, a spin-down luminosity of $L = 5 \cdot 10^{37}$ erg/s and a characteristic age of 1600 y. Therefore it is a comparatively young and energetic pulsar.

MSH 15–5*2* has been observed in the VHE-gamma-ray domain ($E > 100$ GeV) with the `H.E.S.S.` Cherenkov telescope array located in Namibia. The findings published in Aharonian et al. [2005], based on 22.1 hours total observation time, identified the spatially extended emission around the pulsar PSR B1509–58 with the PWN observed in the X-Ray band. Also the SNR shell was ruled out as the main source of the gamma-ray emission. This led to the conclusion that the radiation observed with `H.E.S.S.` was likely inverse Compton emission (1.3.4) related to the X-ray band synchrotron emission of leptonic origin. Based on observations with the Fermi-LAT instrument, Abdo et al. [2010] highly disfavored a hadronic origin of γ-rays due to π^0 decay for the γ-emission of the PWN.

1.2. Observatories

The analysis done by Schöck et al. [2010] and repeated in this work relied on two observatories, `XMM-Newton` and `H.E.S.S.` While the raw data did not change since 2010, a new analysis component for the X-ray data that supplied the input for the model was implemented. Additionally, the model was successfully applied to other objects by Holler [2010] and Willmann [2012], so the basic work flow has been approved. As the starting point, the instruments that gathered the data are introduced.

1.2.1. H.E.S.S.

(a) Photo of the H.E.S.S.-site located in the Khomas region in Namibia.

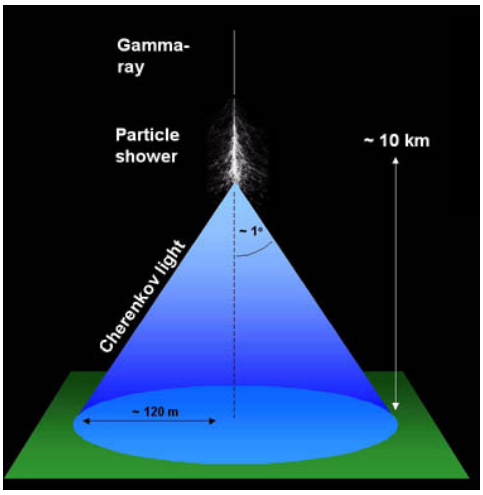

(b) Illustration of the Cherenkov-light emitted by particles of an extended airshower. These can be initiated by γ-rays.

Figure 4: Images by the H.E.S.S. collaboration [http://www.mpi-hd.mpg.de/hfm/HESS/]

The *High Energy Stereoscopic System* (H.E.S.S.) is an array of imaging atmospheric Cherenkov telescopes (IACT) located in Namibia and has been operating since 2002. The name is an allusion to Victor Hess and his balloon flights to determine the elevation-dependence and therefore the origin of cosmic rays. It consists of four 12 m-telescopes (two of them are depicted in Figure 4a) and since 2012 one additional rectangular telescope with an equivalent diameter of 28 m. In the old configuration the field of view was about 0.005 sr with an angular resolution of $\lesssim 0.1\,°$.

The atmospheric imaging technique relies on the fact that charges traveling faster than light in a medium emit what is known as Cherenkov radiation, the optical equivalent of a sonic boom, illustrated in Figure 4b . High-energy photons[3] interact with nuclei in the upper layers of the Earth's atmosphere (8–10 km above ground) to initiate pair production. The resulting particles are then again able to emit bremsstrahlung and therefore initiate a cascade, resulting in an extended air shower. These showers can be detected at the ground as flashes of blueish light lasting only a few nanoseconds. The light pools typically have a radius of about 120 m.

1.2.2. XMM-Newton

XMM-Newton, short for *X-ray Multi-Mirror* is a space-based X-ray observatory launched in 1999 (Figure 5). It is sensitive in the energy range 0.1 keV to 10 keV. As X-rays cannot be reflected or diffracted as readily as visible wavelengths, for each of the three mirror assemblies, 58 mirrors are nested in a Wolter configuration whereby incident photons hit a gold surface at very shallow angles. The outermost mirror has a diameter of 700 mm. The photons are detected by one of several CCD cameras, two front illuminated MOS-Cameras and one back illuminated PN camera

[3] Cosmic rays, most commonly protons, are actually the main source of extended air showers, so background subtraction is a challenging part of operating a γ-ray telescope.

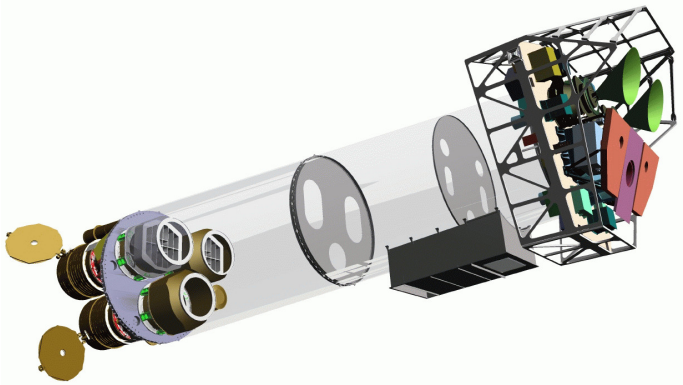

Figure 5: Computer model of the XMM-Newton satellite. The mirror assembly is shown in the lower left hand side, the detectors are located towards the other end of the instrument. Picture by ESA

with a better resolution. The angular resolution is between 4.2" and 6.6", depending on the energy, the field of view is 30′.

To subtract the background e.g. caused by solar wind particles, the CCDs have a variety of filters to block some or all incoming photons, to take background-only images. For more details on the X-Ray setup see Bürkel [2012]. The main selling point of the XMM-Newton observatory is its sensitivity, which makes it ideal to observe faint extended sources. Therefore it is well suited for the task of supplying data for a spatially resolved analysis of the PWN.

1.3. Acceleration and Radiation Mechanisms

Much of the physics of PWNe depends on quite advanced considerations from the fields of plasma and particle physics. Yet some far reaching approximations turn out to be sufficient for most practical purposes when building a model of a PWN. A few relevant key results about the processes taking place are outlined below.

1.3.1. Fermi Acceleration

The description laid out in this section is largely based on Longair [2011]. In the early days of cosmic-ray research, the main concern of researchers was directed at finding an acceleration mechanism which could plausibly explain energies orders of magnitude higher than what thermal radiation can account for. While it is conceivable that e.g. an accretion disk around a black hole might get hot enough to have an emission maximum close to X-ray energies, an object with the peak of the Maxwell-distribution at γ-ray energies would instantly tear itself apart. It was therefore concluded that cosmic rays had to be of *nonthermal* origin. Enrico Fermi proposed a possible solution in 1949. Originally he assumed randomly distributed moving magnetic fields as a means for these particles to gain energy stochastically. For example the magnetic field in molecular clouds distributed throughout the galaxy could act as mirrors on charged particles [Longair, 2011].

(a) (b)

Figure 6: Velocities at a shock front as seen from the rest system of the shock (a) and the rest system of the downstream gas (b)

This approach turned out to be insufficient to explain the observed amount of high energy particles, but the argument Fermi developed can be applied to a shock wave, in the case of a PWN the termination shock, which is responsible for accelerating the particles.

As a basis for the following derivation, a transformation into the rest system of the shock wave is assumed. Therefore gas upstream of the shock enters with the velocity $v_1 = U$, with the velocity of the shock U, and leaves the shock with a velocity v_2. In strong, non relativistic and fully ionized shock waves the equation of continuity

$$\rho_1 v_1 = \rho_2 v_2 \tag{1.7}$$

reduces to

$$v_2 = \frac{1}{4} v_1 \quad . \tag{1.8}$$

Therefore the upstream and downstream rest systems move with a velocity of $V = 3/4 U$ relative to each other (see Figure 6). Assuming a particle crosses the shock front and gets scattered on the other side, after a Lorentz transformation the energy gain is

$$\Delta E = \gamma_V (E + p_x V) - E_0 = pV \cos\theta \quad . \tag{1.9}$$

The shock is assumed to be nonrelativistic ($\gamma \approx 1$), on the other hand the particles are highly relativistic so that $E \approx pc$. Averaging over θ yields a relative energy gain β:

$$\beta = \frac{E}{E_0} = 1 + \frac{4V}{3c} \quad . \tag{1.10}$$

With a probability P the particles cross the shock again and gain the same energy, therefore after k crossings, $N = N_0 P^k$ particles with energies greater than $E = E_0 \beta^k$ remain, the rest escapes the acceleration zone. By a hand-wavy argument, P depends on the shock velocity as $P = 1 - (U/c)$, due to the shock leaving behind the randomly moving particles with velocity $v \approx c$. This allows to derive the energy spectrum of the accelerated particles:

$$\frac{N}{N_0} = \left(\frac{E}{E_0}\right)^{\ln P / \ln \beta} \quad \Rightarrow \quad N(E)\mathrm{d}E \propto E^{-1+\ln P/\ln\beta} \approx E^{-2} \tag{1.11}$$

For a more detailed derivation and explanation see Longair [2011]. For a fully relativistic approach that takes into account magnetic fields in the shock, the derivation is much more complex and often only possible via simulation, yet the obtained results for the spectrum also follow a power law with slightly different spectral index. The empirically determined spectrum of cosmic rays can in fact be described as a power law with a spectral index of −2.7. Therefore a power-law spectrum is the assumed spectrum of high-energy radiation throughout this thesis.

1.3.2. Ion Cyclotron Resonance and Magnetic Recombination

There are, however, additional models that seek to explain further features in the observed radiation. The mechanism proposed by Amato et al. [2006] based on the simulation of magnetized ultrarelativistic shock waves assumes a significant proton (ion) proportion of the energy flow upstream of the shock. In the shock, leptons can then be accelerated by resonant absorption of cyclotron waves within the plasma. Also the work of Pétri et al. [2007] offers a possible explanation of both acceleration and dissipation of Poynting flux into particle flux. At the light cylinder, the magnetic field of the pulsar may in certain geometrical configurations change polarity and recombine at the termination shock, transferring energy to particles. These two mechanisms might be responsible for the break observed in the synchrotron spectrum between the radio and the X-ray band (see section 3.1.1).

Contrary to the approach with an ion component, Spitkovsky [2008] describes a spectrum based on a particle-in-cell simulation of a pure lepton-pair plasma. He derived a relativistic Maxwellian distribution with a power-law tail at higher energies, most likely due to Fermi acceleration. This was deemed as another plausible scenario next to a pure power-law injection spectrum in previous applications of the model to various astronomical objects, e.g. for G0.9+0.1 by Holler et al. [2012]. These examples go to show that there are still a number of unanswered questions about the nature of acceleration in shock waves, but the assumption of a power-law injection spectrum should give a workable estimate.

1.3.3. Synchrotron Radiation

A charged particle in a homogeneous magnetic field with a component perpendicular to the particles momentum vector follows a spiral path with constant pitch angle while emitting electromagnetic radiation [Longair, 2011]. From the finite propagation speed of an electromagnetic disturbance in the case of $v \ll c$ one can derive the energy loss of the particle, which was done by J.J. Thomson in 1906 :

$$-\frac{\mathrm{d}E}{\mathrm{d}t} = \frac{|\ddot{\mathbf{p}}|^2}{6\pi\epsilon_0 c^3} \tag{1.12}$$

Where $\ddot{\mathbf{p}} = q\mathbf{a}$ is the second time derivative of the dipole moment. From eq. (1.12) follows that leptons radiate much more intensely than hadrons at comparable energies as $\mathbf{a}$ is inversely proportional to the mass of the particle. In the relativistic case the energy-loss is related to the Thomson cross section σ_T:

$$-\frac{\mathrm{d}E}{\mathrm{d}t} = 2\sigma_\mathrm{T} c \frac{B^2}{2\mu_0}\beta^2\gamma^2\sin^2\theta \qquad \text{with} \qquad \sigma_T = \frac{e^4}{6\pi\epsilon_0^2 c^4 m_\mathrm{e}^2} \tag{1.13}$$

θ denotes the angle of the velocity with respect to the magnetic field. With the quadratic dependence between the energy loss and the particle's γ-factor, particles with higher energies lose most of their energy quickly and therefore the *synchrotron lifetime* steeply decreases towards higher energies. This is the reason one can observe a time dependent spectral break at radio energies in PWNe: The spectrum of particles that were emitted shortly after the birth of the pulsar gets cut off at increasingly low energies as they radiate outwards, therefore there is an energy threshold at which particles of the PWN can still radiate, yet above this energy, only a decreasing fraction contributes.

In the case of a single particle in a homogeneous field, a sharp emission peak related to the angular frequency can be observed in the non-relativistic case. Due to relativistic distortions which introduce higher harmonics, Doppler-shift and a population of particles with different energies, the synchrotron emission can be broadened into a non Maxwellian continuum. It may still possess a preferred polarization which can be used to deduce the strength and geometry of the magnetic field at the point of emission. For a single particle the first harmonic of emission is given by eq. (1.14).

$$f \approx \frac{\gamma^3 v}{2\pi R_g} \tag{1.14}$$

R_g is the gyro radius of the particle or in the inhomogeneous case the instantaneous curvature of the particle trajectory [Longair, 2011].

As we are looking at a distribution of electrons, we need to relate the electron spectrum to the synchrotron spectrum. Under the assumption of local isotropicity, a distribution of radiating leptons with a power law electron spectrum will result in a power law photon spectrum. The photon index Γ of the emitted synchrotron radiation is related to the spectral index of the leptons as such:

$$\Gamma = \frac{1+p}{2} \quad . \tag{1.15}$$

The exact calculations to obtain this result can be found in Blumenthal et al. [1970].

1.3.4. Inverse Compton Scattering (IC)

This section is based on the lecture notes of Jung [2013]. The inverse Compton effect is related to the normal Compton effect by a Lorentz transformation to the System S^*. Instead of a quasi-free electron being struck by a high energy photon, a high energy electron boosts a photon up towards lower wavelengths. Yet in the rest system of the electron, this is equivalent to a high energy photon striking an electron at rest. Therefore, assuming the photon and the electron move anti-parallel in the lab frame and scatter at an angle of 180° the following applies:

$$E_\gamma^* = \gamma E_\gamma - \gamma(-\beta)E_\gamma\,; \qquad E_\gamma^{*\prime} = \frac{E_\gamma^*}{1+\frac{E_\gamma^*}{m_e c^2}(1-\cos\theta)} \underbrace{\approx}_{E_\gamma^* \ll m_e c^2} E_\gamma^* \tag{1.16}$$

γ is the Lorentz factor of the electron, E_γ the energy of the photon in the lab frame before scattering, $E_\gamma^{*\prime}$ the energy in the rest frame of the electron after scattering. This produces

the photons with the highest observed energies and every source of cosmic radiation with a significant energetic lepton component should be visible in IC-light as the cosmic microwave background provides an ubiquitous target. $E_\gamma^* \ll m_e c^2$ yields a coarse approximation of the attainable energies:

$$E_\gamma^* \ll m_e c^2; E_\gamma \ll \frac{m_e c^2}{4\gamma} \quad . \tag{1.17}$$

For a photon energy of $2{\cdot}10^{-4}$ eV, typical of the CMB, electrons with $E \ll 250$ TeV can be scattered to fulfill the relation, resulting in photon energies of

$$E'_\gamma \approx 4\gamma^2 E_\gamma \ll 20 \text{ TeV} \quad . \tag{1.18}$$

The cross section in this approximation is again related to the Thomson cross section. The formulae (1.13) and (1.19) are in fact of the same form:

$$-\left(\frac{\mathrm{d}E}{\mathrm{d}t}\right)_{\text{Syn}} = -\left(\frac{\mathrm{d}E}{\mathrm{d}t}\right)_{\text{IC}} = 2\sigma_{\text{T}} c \frac{B^2}{2\mu_0} \beta^2 \gamma^2 \sin^2 \alpha \tag{1.19}$$

This is the case because the process of synchrotron radiation can also be described as the Compton scattering of virtual photons of the magnetic field off the moving charge [Longair, 2011]. The average frequency after the scattering took place is given by

$$\langle f \rangle = \frac{4}{3} \beta^2 \gamma^2 \nu_0 \approx \frac{4}{3} \gamma^2 f_0 \quad , \tag{1.20}$$

where f_0 denotes the frequency of the target photon. The reason that the produced radiation lies within a different energy domain as synchrotron radiation from the same particle is that the kinematics allow for light particles such as leptons to transfer a large proportion of their energy to the photons.

2. Observations of MSH 15–52 in High-Energy Bands

Due to the large nonthermal component of the radiation from pulsar wind nebulae, they are most readily observed outside the range of infrared and optical wavelengths in the radio domain as well as the energies beyond ultraviolet radiation. While radio observations of MSH 15–52 played a role in some of the referenced works and therefore have helped to shape the present picture of this object, the data from this thesis are purely derived from observations with `XMM-Newton` (section 2.1) and then compared to observations with `H.E.S.S.` (section 2.2). The following section will focus on this experimental data.

2.1. X-ray Observations

As noted above there has been a long history observing MSH 15–52 in the X-ray band. Attempts to model PWN prior to Schöck [2011] have mostly focused on time dependent features of the

Table 1: Details of the XMM-Newton observations on MSH 15–52. Net exposure time excludes background screening. Table from Bürkel [2012]

Observation ID	Instrument	Exposures [ks]	
		performed	net
0207050201	pn	23.1	12.5
0207050201	MOS1	24.8	15.0
0207050201	MOS2	24.8	14.9
0302730201	pn	14.9	7.3
0302730201	MOS2	16.1	9.2
0302730301	pn	8.2	3.4
0302730301	MOS2	11.7	9.2

PWN's evolution or have been static one-zone models, assuming a constant magnetic field throughout the PWN. The recent availability of higher resolution X-ray data were the starting point for the spatially resolved model implemented by Schöck et al. [2010]. With this model, the changes in the particle spectrum and magnetic field as a function of distance to the pulsar are taken into account, providing a better description, especially of the inner part of the PWN. Details on the three XMM-Newton observations the X-ray analysis employed in this thesis is based on can be found in Table 1. The main difference to the work of Schöck et al. [2010] is that the X-ray data was prepared with a new algorithm for vignetting-correction, the deconvolution of the incidence angle dependent instrument response from the data.

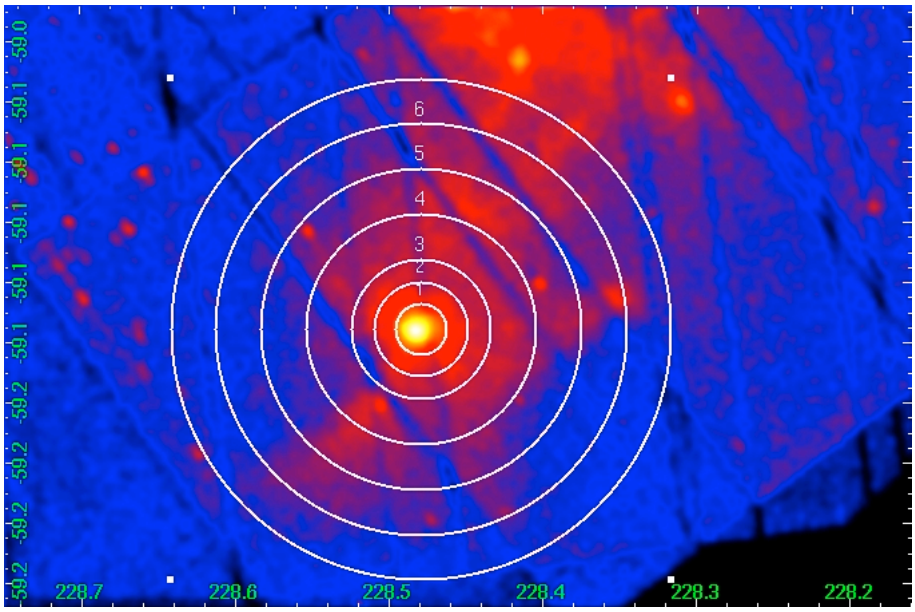

Figure 7: XMM-Countmap of MSH 15–52 from the analysis done by Bürkel [2012]. The data were obtained from three separate observations. The borders of the extraction regions are marked as white circles.

2.1.1. Description of Data Reduction

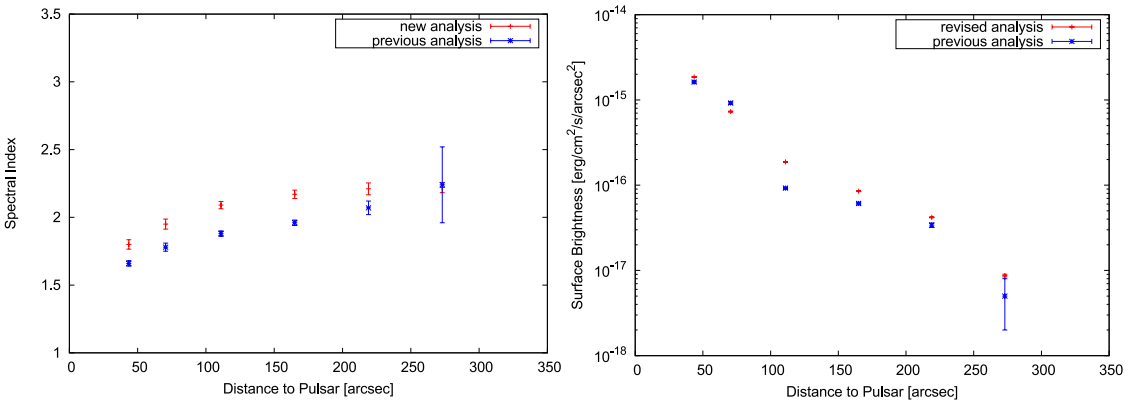

Figure 8: Comparison of the X-ray analysis done by Schöck [2011] (previous analysis) with the recent results of Bürkel [2012] (new analysis).

The X-ray data later used to constrain the model were extracted from the data processed in the scope of Christoph Bürkel's Bachelor thesis [Bürkel, 2012]. In this work, the PWN as shown in Figure 7, was divided into 6 annuli centered on the pulsar and the flux and photon index was extracted for each one. The effective area of the telescope depends both on the distance to the on-axis position and on the energy of incident photons. Therefore the generated raw image is the undistorted image convolved with the instrument response.

In the analysis performed in Schöck et al. [2010] and Schöck [2011], the deconvolution was derived from the observed spatial photon distribution. This introduces noise due to fluctuations in the background and a systematic bias, as the effect of photon energy is neglected [M. Arnaud et al., 2001]. In the same paper, a more favorable approach, whereby each photon is assigned an individual weighting factor, is proposed. This method was used in Bürkel [2012] for the reanalysis of MSH 15–52 in the X-ray band. The difference can be seen in Figure 8. Especially for the faintest annulus number 6 the new method drastically improved the accuracy due to additional data from the MOS cameras. Also the spectral index was found to be higher than previously assumed and more notably, the radial dependence is less steep than with the previous analysis. The surface brightness, directly related to the flux, was found to exhibit an asymptotic flattening towards the outermost regions. Bürkel [2012] provided the explanation that the photon weighting method yields more precise results for high flux variations in the extraction region than the outer annuli or when the effective area notably differs between the background extraction region and the analyzed region.

2.1.2. Data Analysis

The extraction for this thesis started from the cleaned count-per-annulus files from Bürkel [2012]. In this work, the image information was cut according to the extraction regions and processed to make it suitable for determining the flux and photon index of each annulus. As the model needs energetically and spatially resolved flux pivot points in the X-ray band as a point of comparison, the X-ray analysis software `xspec` was used to extract this information [K. Arnaud, 1996]. For that purpose, the existing `xspec`-scripts were used to repeat the fit of an absorbed power law

Table 2: X-ray energy bins used for modeling. The originally intended 6 bins were eventually reduced to 5, by combining bin 5 and 6 into bin 5*.

number	lower bound [keV]	upper bound [keV]
1	0.5	1.75
2	1.75	3
3	3	4.5
4	4.5	6
5	6	7.5
6	7.5	9
5*	6	9

model and an absorbed flux model to the data. The hydrogen abundances to determine column density was taken from the work of Wilms et al. [2000]. Contrary to the earlier analysis, where the first annulus was taken as a benchmark, the absorption column density was fitted as a common parameter for all input data. Additionally to this step already performed by Bürkel [2012], the annuli needed to be divided into energy bins, to provide information about the change in photon index to the model (see Table 2 for the exact division).

Contrary to Bürkel [2012], only data from the PN camera were used in the extraction, even for the least luminous annulus number 6 as using exclusively PN-data was sufficient to reproduce the results from this work and the left over cleaned MOS-files were not suitable for fitting. Also, in the first annulus, the fit did not converge when fitting simultaneously with all three observations. The first two observations alone seemed enough to produce sensible results, therefore observation 3 was left out in this annulus.

Fitting the absorbed power law model to the data with `xspec` failed for the following bins-annulus combinations as the division into energy-bins left too little data for the model: In annulus 1, bin 5 and fitting over the whole energy range; annulus 3, bin 6; annulus 4, bin 6; annulus 5, bin 6; annulus 6, bin 6.

Initially, if only one energy-bin failed to fit, the flux was interpolated by comparing the summed-up flux of the bins with a fit over the whole energy range. In annulus 6, however, the combined flux was incompatible with the summed-up individual fluxes of the energy bins, so therefore this attempt to interpolate the data was discarded.

As an alternative, the energy-bins 6–7.5 keV and 7.5–9 keV were combined into one single bin. In this case, only bin 5 of annulus 1 needed to be interpolated. This breaks direct comparability with the analysis of Schöck et al. [2010] but enabled the generation of physically sensible input for a leptonic model of the PWN. The final data used in the leptonic model are listed in Table 8

2.2. γ-Ray Observations

Remarkably, MSH 15–52 is resolvable as an extended source by the `H.E.S.S.`-array. The angular resolution of imaging atmospheric Cherenkov telescopes is considerably worse than the resolution of X-ray observatories and most PWNe appear point-like or only slightly extended when observed with `H.E.S.S.` In Figure 9, the shape of MSH 15–52 as seen by `H.E.S.S.` is shown.

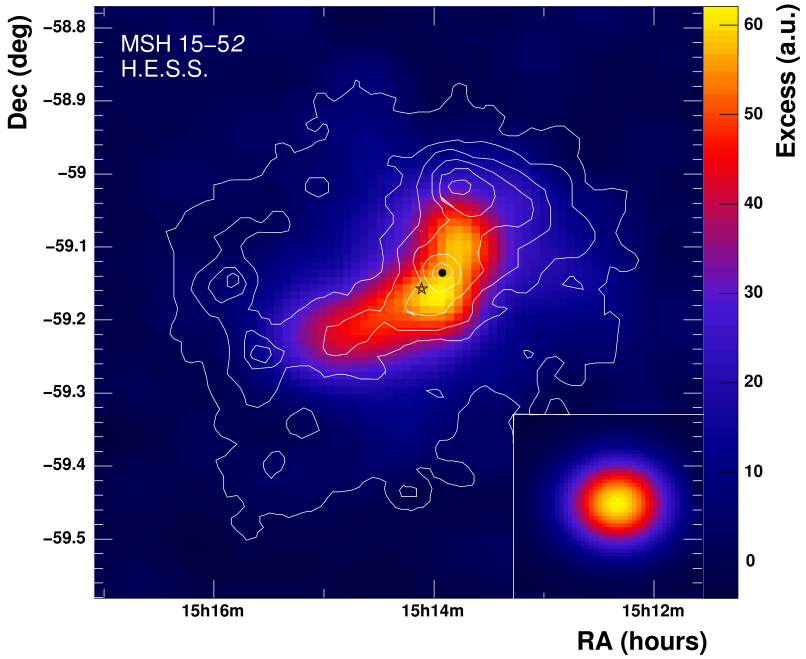

Figure 9: Excess map of MSH 15–52 obtained with H.E.S.S. [Aharonian et al., 2005]. The data were analyzed to yield the best angular resolution, the image was smoothed with a Gaussian Kernel of $\sigma = 0.04°$. The simulated point spread function (PSF) is shown in the lower right corner. The white contours correspond to X-ray observations with ROSAT.

The γ-ray observations were not used in the modeling itself, but as a benchmark for the predictive capabilities for the IC radiation in the VHE domain. Therefore no individual data points or statistics beyond the errors on the flux and the photon index were necessary. No reanalysis was performed, instead the best fitting power law from Aharonian et al. [2005] was used as a yard stick.

In the observed energy range between 280 GeV and ~ 40 TeV the emission is well fitted with $\chi^2/\text{d.o.f} = 13.3/12$ by a power-law function with $\Gamma = 2.27 \pm 0.03_{\text{stat}} \pm 0.20_{\text{sys}}$ and a differential flux of $(5.7 \pm 0.2_{\text{stat}} \pm 1.4_{\text{sys}}) \cdot 10^{-12}\,\text{TeV}^{-1}\,\text{cm}^{-2}\,\text{s}^{-1}$ at 1 TeV [Aharonian et al., 2005].

3. Leptonic Modeling of the PWN

The main focus of this work was to use the X-ray spectra generated from the new analysis to repeat the modeling done in Schöck [2011]. This model follows a top-down approach, where no statement is made about the microscopic interactions inside the nebula, but statistical quantities are modeled on large scales.

3.1. Description of the Model

To model the shape of the measured X-ray spectrum, a static, spherically symmetric model of the PWN is assumed. Of course, clear asymmetries can be observed in the PWN and further out

interactions with the interstellar medium (ISM) and the SNR-shell distort the PWN. Also the age of the leptons increases with distance from the center of the PWN and at some point the change in spin-down luminosity of the of the pulsar becomes relevant. Yet close to the pulsar, younger leptons are steadily supplied and those at X-ray energies or above radiate it away quickly enough to consider the energy output of the pulsar constant. In this region, the synchrotron lifetime of the particles should be much lower than the age of the pulsar to allow for a time independent approach.

The model is based on a starting population of leptons which are then propagated outwards radially. This assumption of spherical symmetry allows for a spatially resolved model based on the annulus shaped extraction regions from the X-ray observations. With each step away from the center, the synchrotron emission is calculated, based on the field configuration. The leptons then enter the next "shell" with reduced energy. The resulting radius dependent spectrum and flux are then compared to the X-ray data for each annulus and the deviation is calculated.

3.1.1. Injection Spectrum

It is assumed that the leptons accelerated by the shock follow a time independent broken power-law distribution, a power law which changes its photon index p at the break energy E_b:

$$Q(E_e) = \begin{cases} Q_0 \left(\frac{E_e}{E_b}\right)^{-p_1} & \text{for} \quad E_e < E_b \\ Q_0 \left(\frac{E_e}{E_b}\right)^{-p_2} & \text{for} \quad E_e \geq E_b \end{cases} \tag{3.1}$$

The model only takes leptons beyond the break energy into account, this approach is justified below. In this case, the spectrum reduces to a simple power law with spectral index p_2. The leptons carry away energy proportional to the spin down luminosity and the energy spectrum $Q(E_e, t)$ of the leptons is time-independent under equilibrium conditions. Thus the normalization constant Q_0 can be computed by using the relation

$$\int_{E_\mathrm{min}}^{E_\mathrm{max}} Q(E_e) E_e \mathrm{d}E_e = \eta L \quad . \tag{3.2}$$

η denotes the efficiency with which the rotational energy of the pulsar is converted into leptons. Because the spectral break is not considered in the model, η is only a lower limit for the conversion efficiency, as the spectral index is less steep prior to E_b. The alternative lepton injection spectrum proposed by Spitkovsky [2008], tested e.g. in Holler et al. [2012], was not modeled in the limited scope of a bachelor thesis due to computation time constraints.

3.1.2. Magnetic Configuration and Energy Limits

The minimum energy relevant for the model E_min is constrained by radio observations and the electron rest mass [Schöck et al., 2010]. As energies below E_b only contribute marginally to the X-ray domain, it is sensible to place the cutoff after the spectral break to simplify the spectral

shape. The limit is set to 1 erg in the following calculations as a safe limit where the contributions fall below the numerical uncertainty.

The derivation of an upper limit for $E_{\max}$ was done by de Jager and Djannati-Ataï [2009]. During the acceleration of the leptons inside the shock, they must remain trapped by the magnetic field, therefore the gyroradius R_g must be no larger than the shock radius R_S. The model parameter ϵ denotes the ratio of these quantities and is expected to be equal to 0.2 at least for Vela-like pulsars with weak shocks [de Jager and Djannati-Ataï, 2009].

$$\epsilon = \frac{R_g}{R_S} \tag{3.3}$$

σ denotes the magnetization at the shock, that is the ratio of electromagnetic energy density to particle density at the shock [Kennel et al., 1984]:

$$\sigma = \frac{F_{\text{Poynting}}}{F_{\text{particle}}} = \frac{B^2}{4\pi\gamma\rho c^2} \quad . \tag{3.4}$$

ρ is the mass density of the particles, $1 < \kappa < 3$ the magnetic compression ratio:

$$\kappa = \frac{|B_{\text{upstream}}|}{|B_{\text{shock}}|} \tag{3.5}$$

[de Jager and Djannati-Ataï, 2009]. The upper boundary of the compression ratio is the limit for very strong shocks [Kennel et al., 1984]. These parameters are strongly correlated, as strong shocks ($\sigma \ll 1$) typically have high compression ratios [Sefako et al., 2003]. In the model, the two parameters are combined into the parameter ξ to take the correlation into account:

$$\xi = \kappa\sqrt{\frac{\sigma}{1+\sigma}} \tag{3.6}$$

For leptons accelerated in the shock front, the gyro radius is given by

$$R_{\text{g}} = \frac{E_{\max}}{eB_{\text{s}}} \quad , \tag{3.7}$$

where B_S is the magnetic field at the shock in Gauss [Harding et al., 1990]. The maximum lepton energy can now be calculated with the magnetic field strength at the shock from Kennel et al. [1984]:

$$E_{\max} = \epsilon\kappa e\sqrt{\frac{\sigma L}{(1+\sigma)c}} = \epsilon e\xi\sqrt{\frac{L}{c}} \quad . \tag{3.8}$$

The second limiting factor for the energy of the leptons injected into the PWN is due to synchrotron losses. Combining the results of 1.3.1 and 1.3.3, the energy gain and synchrotron losses can be compared. The acceleration stops when the losses equal the energy gain. According to de Jager, Harding, et al. [1996] the corresponding maximum energy can then be calculated as:

$$E_{\max} = \gamma_{\max} m_{\text{e}} c^2 = 1.9 \cdot 10^{13} \left(\frac{1}{\langle \sin^2\theta \rangle B_{\text{G}}}\,\text{eV}\right)^{0.5} \quad , \tag{3.9}$$

The magnetic field is given in Gauss, θ is the pitch angle between particles and the magnetic field. For $\langle \sin^2 \theta \rangle = 0.5$ the limit evaluates to:

$$E_{\max} = 43.84 B_S^{-1/2} \,\mathrm{erg} \quad . \tag{3.10}$$

In the model, the lower of both limits is chosen.

3.1.3. Synchrotron Emission and Comparison to Data

To calculate the synchrotron emission from the PWN, a radial particle outflow is presumed where the bulk velocity can be expressed as a power law [Schöck, 2011]:

$$\mathbf{v}(r) = v_S \left(\frac{R_S}{r} \right)^{\alpha} \mathbf{e}_r \quad . \tag{3.11}$$

v_s denotes the velocity with which the shock expands, α is the so called velocity index and determines the rate with which the particles loose energy or are subject to *synchrotron cooling*. A relevant conserved quantity under the assumption of perfect magnetohydrodynamics and a torodial magnetic field is [Kennel et al., 1984]:

$$B v r = B_S v_S r_S = \text{const.} \quad . \tag{3.12}$$

(3.11) and (3.12) can be combined to express the magnetic field in terms of a power law as well:

$$B = B_\mathrm{s} \left(\frac{R_\mathrm{s}}{r} \right)^{1-\alpha} \quad . \tag{3.13}$$

With this, the energy loss of the leptons can be expressed as follows [de Jager, Harding, et al., 1996]:

$$\frac{\mathrm{d}E}{\mathrm{d}t} = -W_\text{adiabatic} - W_\text{synchrotron} = -\frac{E}{3} \nabla \mathbf{v}(r) - 2.368 \cdot 10^{-3} B^2 E^2 \,\mathrm{erg/s} \tag{3.14}$$

$W_\text{synchrotron}$ can simply be derived from eq. (1.13). This differential equation is integrated numerically in discrete steps of r and therefore the emission from each of the resulting shells calculated. Using data of galactic photon fields from the `GALPROP` package (see e.g. Moskalenko [2012]) together with the lepton population, the IC-emission of leptons in each shell can be calculated. The cosmic microwave background (CMB) fields are modeled as Maxwellian distributions with temperature at 2.7 K. Infrared radiation from interstellar dust and starlight are produced by `GALPROP`. To compare this three dimensional data to the two dimensional data of the X-ray analysis, the shells are then projected onto the two dimensional annuli. This method is outlined in Holler et al. [2012].

The criterion of how well a given set of parameters and the resulting synchrotron radiation fits the observational data, is the squared deviation. In the first case, a simple comparison of the measured with the modeled flux F is made $\left(\chi^2_\text{sum}\right)$. The second method is to add an additional factor which emphasizes the relevance of the photon index $\left(\chi^2_\text{alt}\right)$. Δ denotes the error of the respective variable.

$$\chi^2_{\text{flux}} = \sum_i \left(\frac{F_{i,\text{model}} - F_{i,\text{xmm}}}{\Delta F_{i,\text{xmm}}} \right)^2 \tag{3.15}$$

$$\chi^2_{\text{alt}} = \chi^2_{\text{flux}} + \sum_i \left(\frac{R_{i,\text{model}} - R_{i,\text{xmm}}}{\Delta R_i} \right)^2 \tag{3.16}$$

$$\text{with} \quad R_{\text{model|xmm}} = \frac{F_{\text{model|xmm}}(E_{\text{bin1}})}{F_{\text{model|xmm}}(E_{\text{bin5}^*})} \tag{3.17}$$

$$\Delta R_i = \sqrt{\left(\frac{\Delta F_{\text{xmm,i}}(E_{\text{bin1}})}{F_{\text{xmm,i}}(E_{\text{bin5}^*})} \right)^2 + \left(\frac{F_{\text{xmm,i}}(E_{\text{bin1}}) \cdot \Delta F_{\text{xmm,i}}(E_{\text{bin5}^*})}{F^2_{\text{xmm,i}}(E_{\text{bin5}^*})} \right)^2} \tag{3.18}$$

i denotes the number of the annulus, $E_{\text{bin1|bin5}^*}$ the energy of the lowest and highest energy bin, respectively.

Putting it all together, the simulated synchrotron radiation depends on the parameters v_S, ξ η, R_S, ϵ, α and p and to some extend on the number of modeled shells, as well as integration precision. The whole process was implemented by Schöck et al. [2010] using the `H.E.S.S_Paris` framework, one of the software packages to perform data analysis for the `H.E.S.S.`-array, and the library `Modelisation` for ROOT and extended by Holler et al. [2012] and Willmann [2012].

3.2. Parameter Scan

Due to correlations between the model parameters [Schöck et al., 2010] and the fact that there is no feasible analytical form of the model function, standard minimization techniques such as conjugated gradients and Levenberg-Marquardt cannot be applied to this problem. Initial experimentation with alternative algorithms by Schöck [2011] did not look promising, therefore a brute force parameter scan was used. A batch of parameters was evaluated and the best ones selected for the next run, until no further constraint could be achieved.

The computing took place on the "woody"-cluster at the university's data processing center (RRZE) consisting of 212 computer nodes based on Intel "Woodcrest"-chips, with an overall peak performance of 10.4 TFlop/s. One scan consisting of 60,000 evaluations of the model-function required approximately 1100 h of CPU time at a precision of $2 \cdot 10^{-4}$ and 300 shells. At a precision of $5 \cdot 10^{-5}$ and 1000 shells, the most precise setting used in this work, the required CPU time rose to $\sim 10{,}000$ h.

3.2.1. Initial Run

In the first run, the physically reasonable parameter range was scanned. The photon index was fixed to values from the X-ray photon index of the first annulus. With eq. (1.15), the photon index $\Gamma = 1.65 \pm 0.03$ obtained by Bürkel [2012] can be related to an injection spectral index of $p = -2$, which was fixed during the modeling. Also the shock velocity was fixed at 0.3 c, a value that was adopted e.g by Yatsu et al. [2009], in the first three runs. This was necessary to keep the parameter-space to a manageable size.

Table 3: Range of parameters corresponding to input ot the first run of scan 1.

Parameter	minimum	maximum	step-width	unit
Integration Precision	$2 \cdot 10^{-4}$	–	–	–
Number of Shells	300	–	–	–
Injection index (p)	-2.0	-2.0	0	–
Shock radius (R_S)	0.303	0.655	0.044	pc
Shock velocity (v_S)	0.33	0.33	0	c
Combined Sigma Parameter (ξ)	0.001	1.801	0.18	–
radius ratio (ϵ)	0.001	1.751	0.219	–
velocity index (α)	0.01	1.76	0.194	–
conversion ratio (η)	0.001	0.93431	0.104	–

The shock radius (see Table 3) corresponds to scenario II in Schöck et al. [2010], where various previous models or observations were taken into account, resulting in different assumptions about the size of the shock radius. Scenario II was the only scenario evaluated in this thesis, as separate scans would have been prohibitively time consuming and preliminary experimentation seemed to favor the χ^2-values for shock-radii greater than 0.3 parsec. Another reason for the choice is that the model is more sensitive towards underestimation of R_S than to overestimation.

For physical reasons, ξ, α and ϵ can only assume values ranging from 0 to 2 and η from 0 to 1 so the model ranges were chosen accordingly. Yet instead of using a function that linearly spaced values from start to finish, at first a function that excluded the last parameter was used in the generation of the input files[4]. This was not deemed a serious issue as only η shifted towards the excluded value which was included in further iterations. This resulted in 40000 separate evaluations of the model function, with ranges and spacing as in Table 3.

First, all the results where one of the χ^2 methods yielded "inf" or "nan" were discarded. This may be the case when dividing by zero or a value overflows for very divergent parameters. Then the union of parameter ranges for sets with $\chi^2_{\text{alt}} < 1500$ (25 sets remaining) and $\chi^2_{\text{sum}} < 2000$ (42 sets remaining) was chosen as constraint region for run number 2. This differs from the criterion later chosen in the scanning process. In the following runs, the region of parameter space in which the best 10% of χ^2 fell was chosen as the range for the next iteration. The deviation in run 1 was necessitated by the fact that for the first set of parameters this method excluded all but one parameter set for the χ^2_{sum} and three for χ^2_{alt}, respectively. We assumed that this was a too small sample, thus the rather arbitrary method to obtain a larger sample of parameter sets was used for the input generation for iteration number two.

3.2.2. Coarse parameter Constraint

After five iterations of the scan with an eventual integration precision of $5 \cdot 10^{-5}$ and a number of shells of 1000, no further constraint in the parameter space could be determined with the available computing power. The values for precision and number of shells were close to those determined by Holler [2010] as the most precise setting that still had an impact on the value of χ^2.

[4] `numpy.arange(start, stop, stepwidth)` instead of `numpy.linspace(start, stop, n)`

Table 4: Best parameter sets after the 5th scan iteration.

p	R_S[pc]	v_S[c]	ξ	ϵ	α	η	χ^2_{alt}	χ^2_{sum}
2	0.710	0.38	0.358	0.165	1.498	1	1012	654
2	0.710	0.33	0.317	0.100	1.52	1	904	761

Table 5: Best parameter sets from the second scan with constrained η.

p	R_S[pc]	v_S[c]	ξ	ϵ	α	η	χ^2_{alt}	χ^2_{sum}
−2	0.756	0.33	0.23	0.2	1.714	0.7	1296	1100
−2.0	0.756	0.38	0.307	0.2	1.671	0.7	1335	1024

The final constraints are shown in Table 6. During the scan, the shock velocity was varied after the other parameters were reasonably constrained and the shock radius was allowed to drift out of the original bounds as there are no clear physical limits given for this parameter, but earlier simulations in Yatsu et al. [2009] and Gaensler, Arons, et al. [2002].

The best set of parameters for χ^2_{sum} and χ^2_{alt} for run 1 are listed in Table 4.

What meets the eye, is that the efficiency η drifts to values close to 1. It seems dubious that the efficiency could actually reach this value, as the energy of the electromagnetic field responsible for accelerating the particle flux would have to be converted nearly completely into leptons. A first hypothesis was that a local minimum was hiding in the slope of the η-χ^2 dependence that was excluded too soon in the earlier iterations of the scan.

3.2.3. Second Scan

Therefore a second scan was performed, starting with the original parameter space, but confining η between 0 and 0.7, a shot in the dark as to where an alternative, better fitting η might be located. Schöck et al. [2010] or Schöck [2011] provided only a lower limit of 0.3 for the parameter, so a sensibility check with earlier data was not possible. The scan was done with 200,000 parameter sets in the first iteration, a lot more than in scan 1. Yet again η converged to the maximum allowed value of 0.7 and the scan did not uncover any additional minima. Therefore only a second run to refine the parameters coarsely was performed. The best sets are listed in Table 5.

Additionally, a few parameter sets which produced the lowest χ^2 in the first scan were evaluated again, with a step width in η of 0.05 over the interval $[0,1]$. This is plotted in Figure 10 for the parameter sets from section 3.2.2. Also with different parameters a similar picture emerged: When fixing the other parameters, to obtain the η dependence in a slice of the parameter space, χ^2 strictly decreased with increasing η.

Tanaka et al. [2010] and Martín et al. [2012] arrived at similar values in their time dependent modeling of multiple young PWN. This should be taken with a grain of salt though, as this thesis uses the model in the state used by Willmann [2012] without meaningful modifications. Holler [2010] found $0.38 < \eta < 0.55$ for the PWN G0.9+0.1 while Tanaka et al. [2011][5] found $0.001 < \eta < 0.003$ for G0.9+0.1. Therefore current models seem to allow a wide range for the conversion efficiency and no real statement can be made if the value for this parameter is sensible based on the literature.

[5] In [Tanaka et al., 2010] "η" is defined as $\dot{E}_{\text{mag}}(t) = \eta \dot{E}_e(t)$, 1-$\eta$ with respect to the definition in this thesis

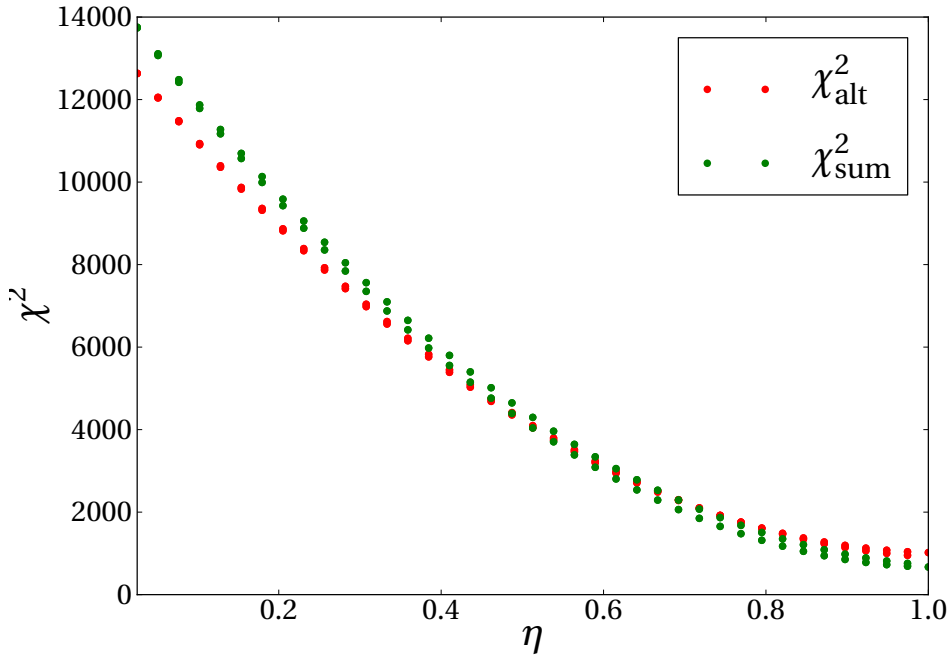

Figure 10: η versus χ^2 for the two parameter sets that yielded the best χ^2 values in scan 1. This plot is characteristic for the dependence between χ^2 and η. The minimum in both cases lies at $\eta = 1$.

Somewhat surprisingly, the VHE Data is marginally better predicted by the second scan run with $\eta = 0.7$ when compared to the first with $\eta = 1$, despite the worse fit in the X-ray band.

3.3. Results of the Modeling

Comparing the parameter constraints of scan 1 to the results of Schöck et al. [2010] is not directly possible, as the exact methodology to arrive at the parameter constraints was not stated in the quoted work. In Scenario II, the shock radius was fixed to 0.5 pc, while in the present work it was subject to optimization. The best set of parameter selected for some plots in Schöck [2011] used values of $\alpha = 0.47$ and $\xi = 0.56$, which differ significantly from the range obtained here. Also the

Table 6: Range of parameters after the 5th scan iteration

Parameter	minimum	maximum	step-width	unit
Integration Precision	$5 \cdot 10^{-5}$	–	–	–
Number of Shells	1000	–	–	–
Injection index (p)	−2.0	−2.0	0	–
Shock radius (R_S)	0.597485	0.710175	0.0188	pc
Shock velocity (v_S)	0.23	0.43	0.04	c
Combined Sigma Parameter (ξ)	0.15	0.4	0.00357	–
radius ratio (ϵ)	0.1	0.49	0.0557	–
velocity index α	1.45	1.57	0.02	–
conversion ratio η	0.93	1	0.01	–

second scenario with $\eta = 0.7$ is incompatible with the results of Schöck et al. [2010]. Inspecting this slice of parameter space with the available data did not reveal the existence of an additional minimum that was missed in the scan.

Comparing the computed results depicted in the following plots and the results from Schöck et al. [2010], the model overestimated the photon index for the outer regions in both analyses, even with very different parameter sets. This is accentuated by the fact that with the new X-ray data, the measured radial dependence of the photon index became less steep and even seems to flatten out. The compromises that where taken during the X-ray data extraction are of course somewhat of a game changer and deviations are therefore expected.

The following plots were created from the best datasets according to χ^2_{sum} from scan 1 and scan 2.

It is not surprising that the surface-brightness plots in Figure 11, are virtually indistinguishable, as both parameter sets were optimized to the flux. The model can explain the surface brightness of MSH 15–5*2* in the X-ray band reasonably well, as it is unreasonable to assume a model with 6 degrees of freedom can be matched to 36 pivots (Table 8) down to one standard deviation. While the model intrinsically predicts a smooth decay of the surface brightness, the data show scattering, which is expected as MSH 15–5*2* does have asymmetric features.

The photon index, shown in Figure 12 differs notably between the two valuated scenarios, the $\eta = 1$ scenario is better suited for predicting the photon index. In both cases the model predicts a lower index for the inner annuli and a much higher increase towards the outer regions as measured. This large deviation would justify relying mainly on the χ^2_{alt} criterion in further applications of the model to avoid arriving at too large photon indices. As the bad fit towards the outer regions was already present in Schöck [2011], this effect might be intrinsic to the model.

The computed spectral energy distributions (SEDs) in Figure 13 span a much wider energy range than the photon index and surface brightness plots, as the whole frequency spectrum has been extrapolated by the model. In this type of representation, the photon flux versus energy is plotted logarithmically and the distribution is multiplied by E^2. This compensate the slope a photo index of -2 would produce and to converts the particle flux into an energy flux. This is a common method of plotting spectral features over many orders of magnitude of energy. The two main features in the plots produced during this thesis are the two peaks, corresponding to the synchrotron radiation, covering radio, optical and X-ray energies and the IC peak at γ-ray energies.

The computed IC emission is compatible with the flux obtained from `H.E.S.S.` observations. The shape of the the SED does not change by much around the best set of parameters. In Figure 14 the very similar SEDs are plotted together to make the difference discernible.

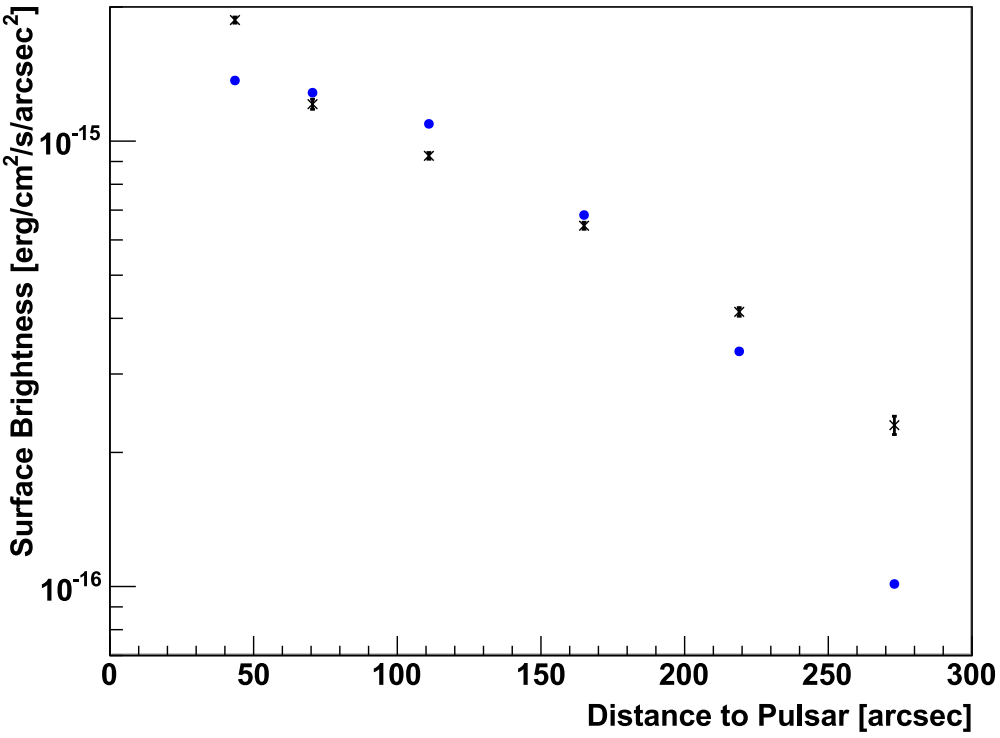

(a) $\eta = 1$

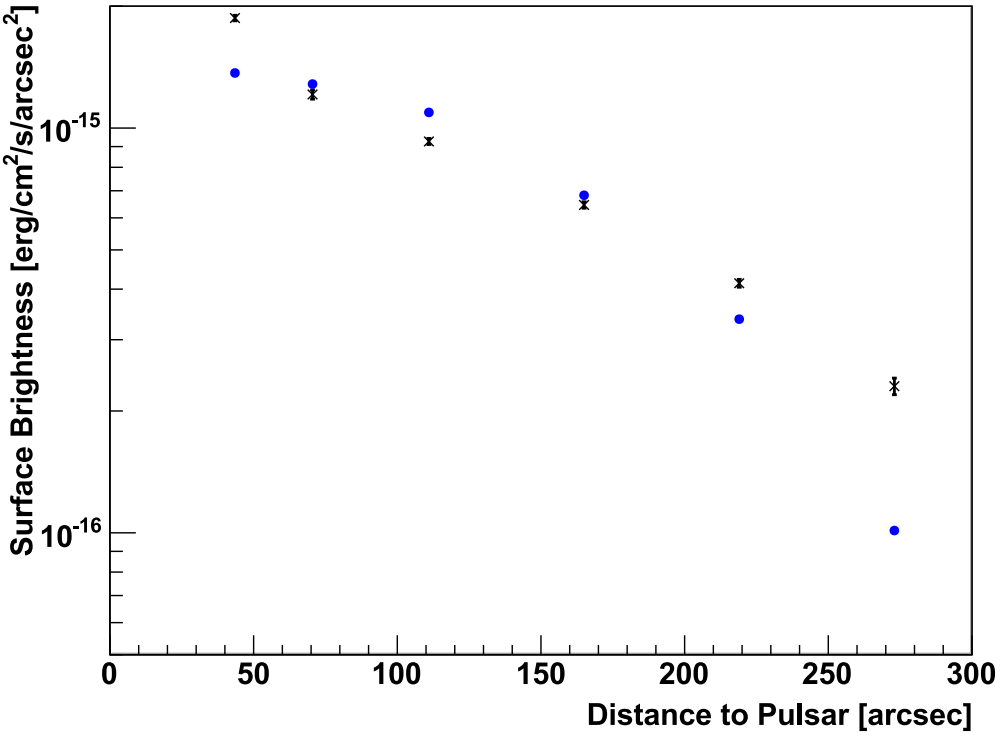

(b) $\eta = 0.7$

Figure 11: Modeled (blue) and measured (black) surface brightness for the 6 annuli in the energy range from 0.5 keV to 9 keV, the range covered by `XMM-Newton`.

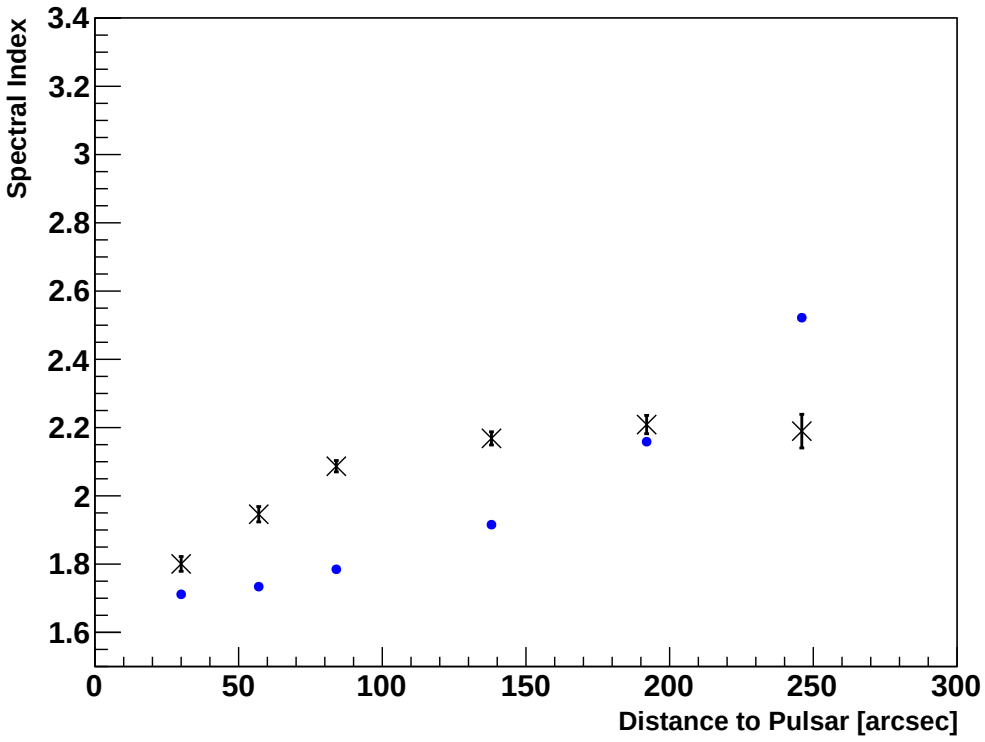

(a) $\eta = 1$

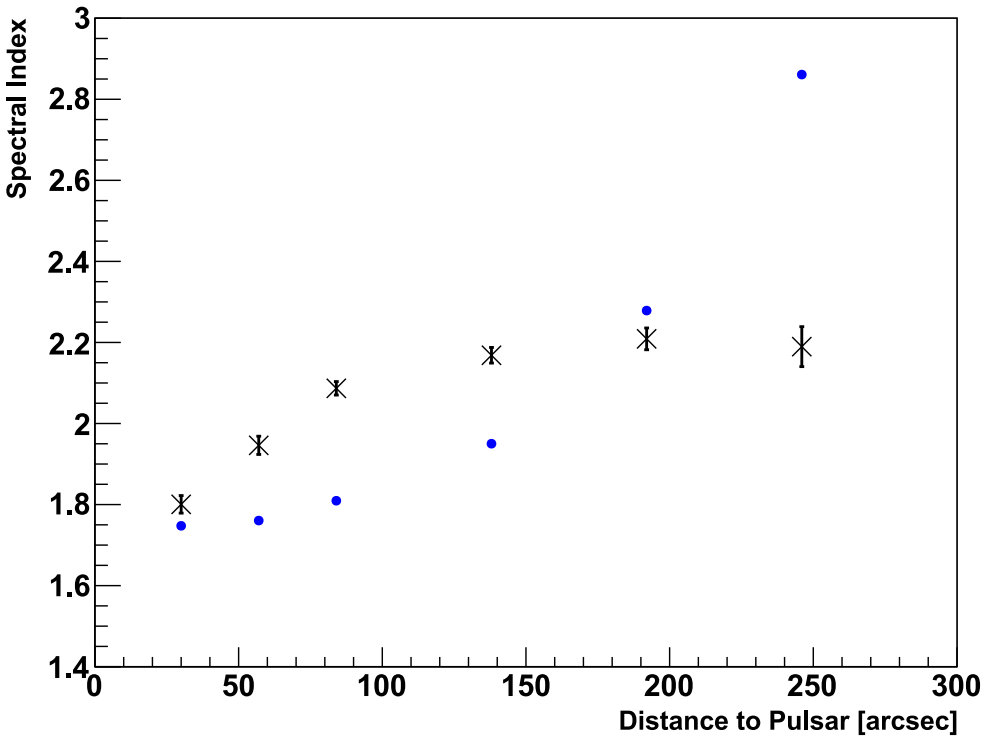

(b) $\eta = 0.7$

Figure 12: Modeled (blue) and measured (black) photon index for the 6 annuli in the energy range from 0.5 keV to 9 keV, the range covered by `XMM-Newton`.

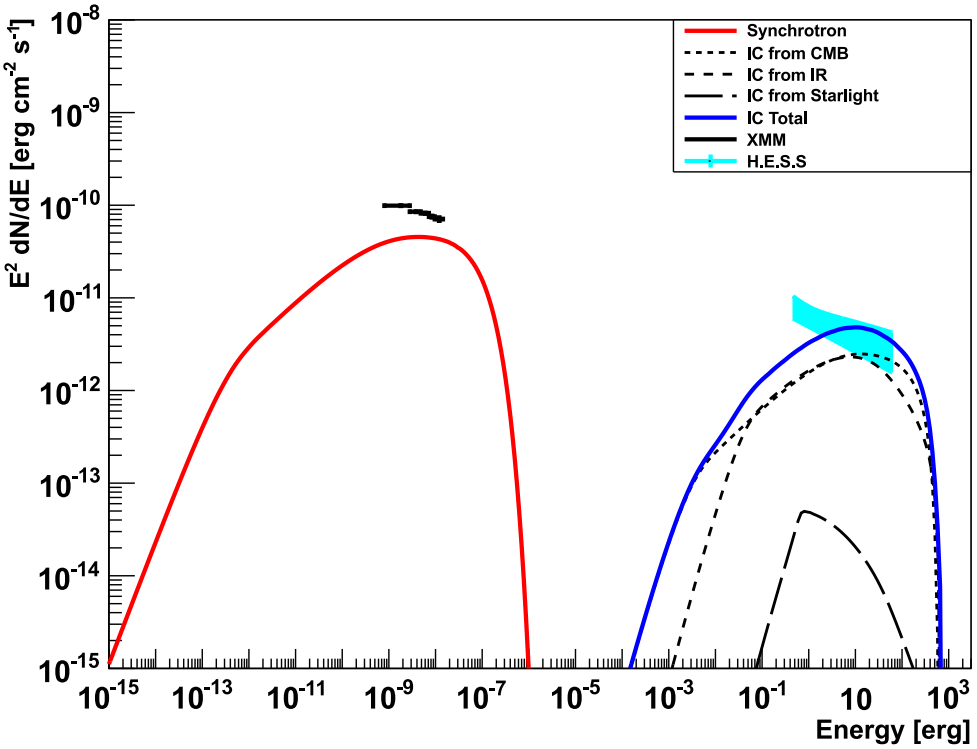

(a) $\eta = 1$

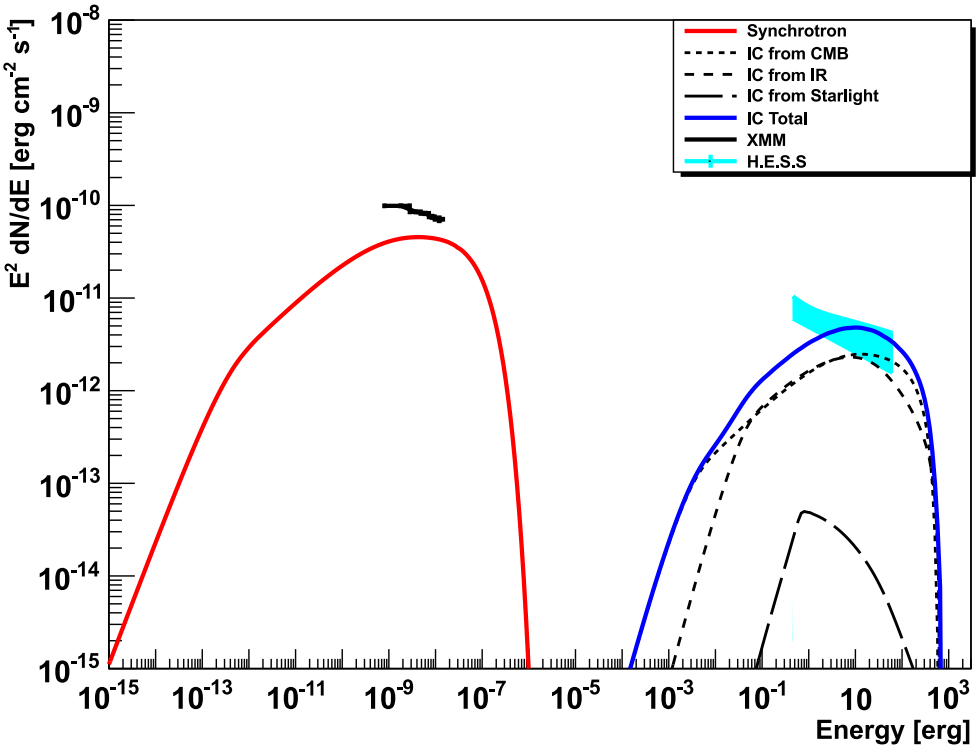

(b) $\eta = 0.7$

Figure 13: Spectral energy distribution for the model and measured data

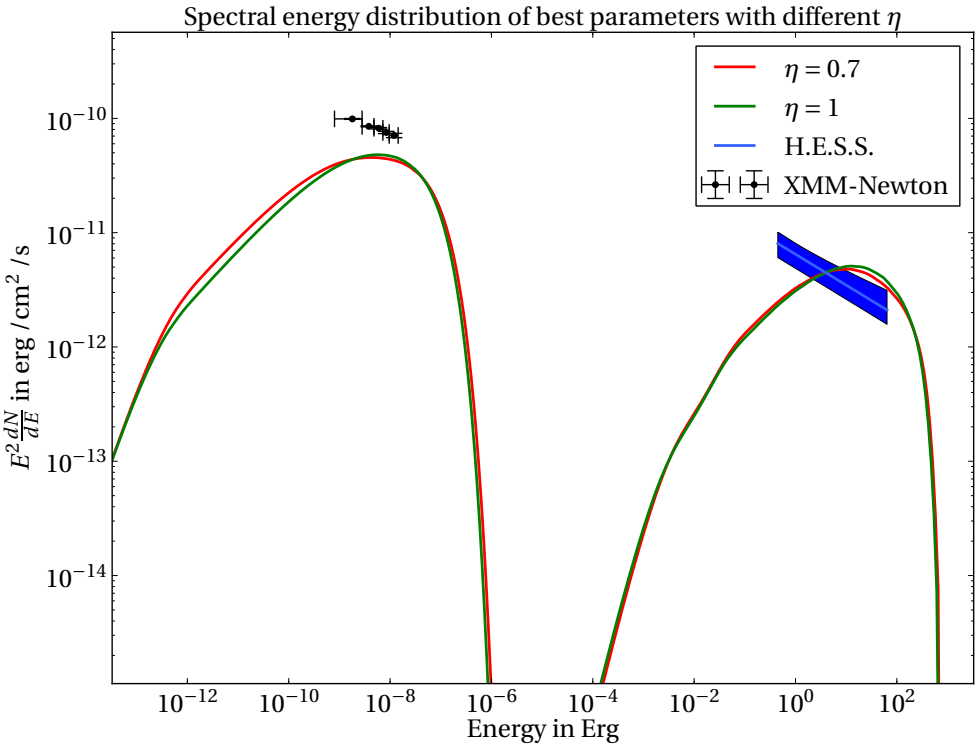

Figure 14: Comparison of the SEDs for $\eta = 1$ and $\eta = 0.7$.

A really troublesome feature of all the modeled SEDs obtained in this work is that they are displaced from the X-ray data by about half an order of magnitude. Yet this should definitely not be the case, as the model is designed to offer the best fit to the X-ray data and the comparatively low χ^2_{sum} does not suggest a deviation on this scale. On the off chance that this behavior is not a fluke of the data conversion or plotting procedure, it might offer some insight into the behavior of η. A constant offset in flux should clearly favor model parameters that increase the flux globally. Increasing η is a way to increase the total flux and might arise when the model underestimates the energy output of the pulsar and choosing a high η partially compensates for this.

As the spin down luminosity can be measured with much greater relative accuracy than the X-ray or γ-ray emission, it is unlikely that this is a problem of that particular measurement, but an artifact of the modeling procedure for this particular set of X-ray data. But there could nevertheless be a deeper reason for the bad fit in the SEDs apart from human error. Still the most likely explanation is that some conversion factor was missed in exporting the data for the SEDs, as the surface brightness plots generated in the same function call do not show this constant offset. It is unlikely that the plotting routines are at fault and the fluke can be attributed to the exported data as the plots in Figure 13 and Figure 14 were done with different tools and independent of each other.

4. Conclusion and Outlook

4.1. Summary

In this thesis the steps necessary to prepare the input data from the X-ray analysis of MSH 15–5*2* presented in Bürkel [2012] were carried out and the model adopted from Schöck [2011] was reapplied to the PWN using the new X-ray data. First a general introduction into the physics of pulsars, their pulsar winds and PWNe was given followed by a more detailed discussion of the object of interest, MSH 15–5*2*. A discussion of the two instruments that provided the basis for the performed analysis, `H.E.S.S.` and `XMM-Newton` followed. A short outline of the relevant acceleration and radiation mechanisms concluded the theoretical part. Based on that foundation, the process of data extraction and reduction was introduced. The data extraction proved to be problematic as some observational data were unusable and the division into energy bins produced insufficient statistic in some cases. Therefore only a reduced ammount of data was generated.

The methodology of the static, spatially resolved model used in this thesis, the relevant model parameters and the relation to other simulation approaches was discussed in detail. Two scenarios with different constraints on the parameter η were evaluated. While no final verdict concerning the behavior of η could be deduced, the interesting possibility arises that with the new data the current implementation of the underlying assumptions of the model reach their limits when it comes to predicting the X-ray flux. In the end the surface brightness of MSH 15–5*2* can be reproduced, but not the photon index. While the simulated IC-spectrum is compatible with γ-ray data, the two scenarios produced remarkably similar results, but both showing a mysterious deviation from the X-ray domain. In a nutshell, the modeling revealed some conflicting results and a definitive deviation from measured data both for the photon index and the outer regions of the PWN. There might, however, be purely technical reason for the apparent shortcomings and thus an outlook of technicalities that could be improved in the future and opportunities for further research that are discussed in the last section.

One of the key aspects of science is that every question answered raises at least one further question. While many of the questions raised by this thesis are of technical nature, revisiting the leptonic modeling of MSH 15–5*2* also unveiled some rather intriguing physical conundrums. The attempt to disentangle those two fields from each other went beyond the scope of this thesis, nevertheless a few paths of further investigation became apparent.

4.2. Exclusion of Annulus Number 6

What becomes clear from Figure 11 and Figure 12 is that the model is unable to explain the measured emission from annulus 6 within the given physical bounds. As Bürkel, 2012 hinted in his thesis, the X-ray data extraction proved problematic for this annulus, but the steps to add the MOS data could not be reproduced for this work. Therefore to exclude the probably unsuitable dataset, the scan was repeated for the 5 inner annuli. Only preliminary results could be extracted, listed in Table 7, as the simulation was still running towards the deadline of this thesis. As the outer regions proved to be problematic with the old analysis as well, it might generally be the better choice to apply the model only to the inner region of the PWN. Problems

Table 7: Preliminary parameter constraints for scan 3 with excluded annulus number 6. The χ^2 values lie in a comparable range with $\chi^2_{\text{sum}} = [817, 1185]$ and $\chi^2_{\text{alt}} = [670, 943]$ as the previous scans. For the final result they are expected to fall significantly below the value from the previous scans, as the one annulus with the highest deviation is not included in the summation.

Parameter	minimum	maximum	step-width	unit
Integration Precision	$2 \cdot 10^{-4}$	–	–	–
Number of Shells	300	–	–	–
Injection index (p)	−2.1	−1.9	0.05	–
Shock radius (R_S)	0.579838	0.655469	0.0063	pc
Shock velocity (v_S)	0.28	0.4	0.12	c
Combined Sigma Parameter (ξ)	0.2	0.3	0.01	–
radius ratio (ϵ)	0.25	0.475	0.05	–
velocity index α	1.445	1.625	0.03	–
conversion ratio η	0.84	1	0.02	–

with the outermost annulus also arose during the modeling in Holler [2010] and as a result, that region was discarded.

4.3. Further Considerations

It remains unclear if the problems during the X-ray analysis described in section 2.1.2 were due to too generous cutting of the data or other shortcomings in previous steps of the X-ray analysis or if the three PN observations of MSH 15–5*2* combined with the Arnaud-binning method intrinsically deliver insufficient statistics. Yet as repeating the steps in the X-ray analysis were not the objective of this thesis, this hypotheses seem very unlikely. A possible solution to this conundrum might be that the method of generating multiple `xspec` scripts, one for each annulus energy bin combination, breaks the simultaneous fit of the absorption density and the fit fails to produce sensible results for some combinations where too few events are left. In summary, at least a X-ray reanalysis based on the observations used here should be attempted to determine if the extraction in this thesis was performed correctly.

As pointed out in Schöck [2011], due to long background flaring periods, the net exposure time for the X-ray observations is below 6 ks after background cleaning. Longer observation time or combining data from various observatories would certainly allow for better statistics, even with conservative cuts applied to the X-ray data. A further valuable tool for the refinement of the modeling and data analysis may be provided by data from additional energy domains, e.g. the HE-γ domain covered by the Fermi-LAT Observatory. Using this data as a second benchmark for the computed SED, might reveal further details about the predictive capability of the model [Aharonian et al., 2005].

Creating an analysis chain that, once implemented, can be understood and rerun without extensive manual intervention might seem cumbersome at first. Making the code written during scientific research publicly available, ideally releasing it under a copyleft licence, would certainly allow for more rapid progress and allow others to benefit from ones work, as the hurdles to reapply the existing tools to a new problem should then be very small.

Even though the author does not have much knowledge in optimization techniques, the nagging feeling remains, that there is a faster and more reliable way to compute the best parameter set than trial and error with a rather arbitrary 10% criterion. Expensive black-box functions without derivative information are generally hard to optimize globally. The computation time necessary to perform a brute force scan was a major factor constraining the scope of this thesis. There are optimization methods that might be worth a second glance, for example using response surfaces to generate new sampling points, as first described in Jones et al. [1998]. Even though this might not strictly speaking in the scope of astrophysics, an investigation for optimizing the modeling procedure has the potential to greatly accelerate future research in this area.

5. Acknowledgments

Primarily, thanks to my reviewers, Gisela Anton and Ira Jung for suggesting this interesting topic and for the work of grading this thesis.

A big “thank you!” goes to my advisors Kathrin Valerius and Philipp Willmann for their patience with my stubbornness and at times incompetence and for putting up with my lamentations about poor programming while only producing marginally better code.

Also thanks everyone in the H.E.S.S. working group and ECAP at large for the warm welcome and Susanne Raab for a very pleasant working atmosphere in the office and quick availability for questions.

Of course I would also like to thank my proofreaders and/or LaTeX consultants, Simon Weiß, Johannes Hielscher and Max Rumler for their detailed and sometimes harsh, but very helpful criticism.

This research has made use of NASA’s Astrophysics Data System.

References

Abdo, A. A. et al. (May 2010). "Detection of the Energetic Pulsar PSR B1509-58 and its Pulsar Wind Nebula in MSH 15-52 Using the Fermi-Large Area Telescope". In: *The Astrophysical Journal* 714, pp. 927–936. DOI: 10.1088/0004-637X/714/1/927. arXiv: 1003.3833 [astro-ph.HE] (cit. on p. 5).

Aharonian, F. et al. (May 2005). "Discovery of extended VHE gamma-ray emission from the asymmetric pulsar wind nebula in MSH 15-52 with HESS". In: *Astronomy an Astrophysics* 435, pp. L17–L20. DOI: 10.1051/0004-6361:200500105. eprint: arXiv:astro-ph/0504120 (cit. on pp. 5, 15, 29).

Amato, E. and Arons, J. (Dec. 2006). "Heating and Nonthermal Particle Acceleration in Relativistic, Transverse Magnetosonic Shock Waves in Proton-Electron-Positron Plasmas". In: *The Astrophysical Journal* 653, pp. 325–338. DOI: 10.1086/508050. eprint: arXiv:astro-ph/0609034 (cit. on p. 9).

Arnaud, K. A. (1996). "XSPEC: The First Ten Years". In: *Astronomical Data Analysis Software and Systems V*. Ed. by G. H. Jacoby and J. Barnes. Vol. 101. Astronomical Society of the Pacific Conference Series, p. 17 (cit. on p. 13).

Arnaud, M. et al. (2001). "Measuring Cluster Temperature Profiles with XMM/EPIC". In: *Astronomy and Astrophysics, Volume 365, Number 1* (cit. on p. 13).

Blumenthal, George R. and Gould, Robert J. (Apr. 1970). "Bremsstrahlung, Synchrotron Radiation, and Compton Scattering of High-Energy Electrons Traversing Dilute Gases". In: *Rev. Mod. Phys.* 42 (2), pp. 237–270. DOI: 10.1103/RevModPhys.42.237. URL: http://link.aps.org/doi/10.1103/RevModPhys.42.237 (cit. on p. 10).

Bürkel, Christoph (2012). "Spatially resolved X-ray spectroscopy of the pulsar wind nebula MSH 15–5*2* ". Bachelor Thesis. Friedrich-Alexander-Universittät Erlangen-Nürnberg (cit. on pp. 7, 12 sqq., 19, 28).

de Jager, O. C. and Djannati-Ataï, A. (2009). "Implications of HESS Observations of Pulsar Wind Nebulae". In: Astrophysics and Space Science Library 357. Ed. by W. Becker, p. 451. DOI: 10.1007/978-3-540-76965-1_17. arXiv: 0803.0116 (cit. on p. 17).

de Jager, O. C., Harding, A. K., et al. (Jan. 1996). "Gamma-Ray Observations of the Crab Nebula: A Study of the Synchro-Compton Spectrum". In: *The Astrophysical Journal* 457, p. 253. DOI: 10.1086/176726 (cit. on pp. 17 sq.).

Gaensler, B. M., Arons, J., et al. (Apr. 2002). "Chandra Imaging of the X-Ray Nebula Powered by Pulsar B1509-58". In: *The Astrophysical Journal* 569, pp. 878–893. DOI: 10.1086/339354. eprint: arXiv:astro-ph/0110454 (cit. on p. 21).

Gaensler, B. M., Brazier, K. T. S., Manchester, R. N., Johnston, S., and Green, A. J. (May 1999). "SNR G320.4-01.2 and PSR B1509-58: new radio observations of a complex interacting system". In: *MNRAS* 305, pp. 724–736. DOI: 10.1046/j.1365-8711.1999.02500.x. eprint: arXiv:astro-ph/9901262 (cit. on p. 4).

Gaensler, B. M. and Slane, P. O. (2006). "The Evolution and Structure of Pulsar Wind Nebulae". In: *Annual Review of Astrophysics* (cit. on pp. 1, 3 sq.).

Harding, A. K. and Gaisser, T. K. (Aug. 1990). "Acceleration by pulsar winds in binary systems". In: *The Astrophysical Journal* 358, pp. 561–574. DOI: 10.1086/169009 (cit. on p. 17).

Heger, A., Fryer, C. L., Woosley, S. E., Langer, N., and Hartmann, D. H. (2003). "How Massive Single Stars End Their Life". In: *The Astrophysical Journal* 591.1, p. 288 (cit. on p. 1).

Holler, Markus (2010). “Spatially Resolved X-Ray Analysis and Modeling of the Non-Thermal Emission of the Pulsar Wind Nebula G0.9+0.1”. Diploma Thesis. Friedrich-Alexander-Universittät Erlangen-Nürnberg (cit. on pp. 5, 20 sq., 29).

Holler, Markus et al. (2012). “Spatially resolved X-ray spectroscopy and modeling of the nonthermal emission of the pulsar wind nebula in G0.9+0.1”. In: *Astronomy & Astrophysics* (cit. on pp. 9, 16, 18 sq.).

Jones, Donald R., Schonlau, Matthias, and Welch, William J. (Dec. 1998). “Efficient Global Optimization of Expensive Black-Box Functions”. In: *J. of Global Optimization* 13.4, pp. 455–492. ISSN: 0925-5001. DOI: 10.1023/A:1008306431147. URL: http://dx.doi.org/10.1023/A:1008306431147 (cit. on p. 30).

Jung, Ira, ed. (2013). *Lecture: Einführung in die Gammaastronomie* (cit. on p. 10).

Kaspi, V. M., Manchester, R. N., Siegman, B., Johnston, S., and Lyne, A. G. (Feb. 1994). “On the spin-down of PSR B1509-58”. In: *The Astrophysical Journal Letters* 422, pp. L83–L86. DOI: 10.1086/187218 (cit. on p. 5).

Kennel, C. F. and Coroniti, F. V. (Aug. 1984). “Confinement of the Crab pulsar’s wind by its supernova remnant”. In: *The Astrophysical Journal* 283, pp. 694–709. DOI: 10.1086/162356 (cit. on pp. 17 sq.).

Longair, Malcom S. (2011). *High Energy Astrophysics*. Cambridge University Press (cit. on pp. 2 sq., 7, 9 sqq.).

Manchester, R. N., Tuohy, I. R., and Damico, N. (Nov. 1982). “Discovery of radio pulsations from the X-ray pulsar in the supernova remnant G320.4-1.2”. In: *The Astrophysical Journal Letters* 262, pp. L31–L33. DOI: 10.1086/183906 (cit. on p. 5).

Martín, J., Torres, D. F., and Rea, N. (Nov. 2012). “Time-dependent modelling of pulsar wind nebulae: study on the impact of the diffusion-loss approximations”. In: *MNRAS* 427, pp. 415–427. DOI: 10.1111/j.1365-2966.2012.22014.x. arXiv: 1209.0300 [astro-ph.HE] (cit. on p. 21).

Mills, B. Y., Slee, O. B., and Hill, E. R. (Dec. 1961). “A Catalogue of Radio Sources between Declinations -50° and -80°”. In: *Australian Journal of Physics* 14, p. 497. DOI: 10.1071/PH610497 (cit. on p. 5).

Moskalenko, I. (July 2012). “Modeling cosmic ray propagation and associated interstellar emissions”. In: *39th COSPAR Scientific Assembly*. Vol. 39. COSPAR Meeting, p. 1281. arXiv: 1105.4921 [astro-ph.HE] (cit. on p. 18).

Pétri, J. and Lyubarsky, Y. (Oct. 2007). “Magnetic reconnection at the termination shock in a striped pulsar wind”. In: *Astronomy & Astrophysics* 473, pp. 683–700. DOI: 10.1051/0004-6361:20066981 (cit. on p. 9).

Schöck, F. M. (2011). “A Detailed Study of the Pulsar Wind Nebula MSH 15–52 in X-rays and TeV γ-rays”. PhD thesis. Friedrich-Alexander-Universittät Erlangen-Nürnberg (cit. on pp. 11, 13, 15, 18 sq., 21 sqq., 28 sq.).

Schöck, F. M., Büsching, I., Jager, O. C. de, Eger, P., and Vorster, M. J. (2010). “Spatially resolved XMM-Newton analysis and a model of the nonthermal emission of MSH 15–52”. In: *Astronomy & Astrophysics* (cit. on pp. 4 sq., 12 sqq., 16, 19–23).

Sefako, R. R. and de Jager, O. C. (Aug. 2003). “Constraints on Pulsar Magnetospheric and Wind Parameters for the Compact Nebulae of Vela and PSR B1706-44”. In: *The Astrophysical Journal* 593, pp. 1013–1023. DOI: 10.1086/376567. eprint: arXiv:astro-ph/0305119 (cit. on p. 17).

Slane, P. O. (2005). “The devil is in the details: Compact structures in pulsar wind nebulae”. In: *Advances in Space Research 35 (2005) 1092–1098* (cit. on p. 3).

Slane, P. O. et al. (Apr. 2000). “Chandra Observations of the Crab-like Supernova Remnant G21.5-0.9”. In: *The Astrophysical Journal Letters* 533, pp. L29–L32. DOI: 10.1086/312589. eprint: arXiv:astro-ph/0001536 (cit. on p. 4).

Spitkovsky, A. (July 2008). “Particle Acceleration in Relativistic Collisionless Shocks: Fermi Process at Last?” In: *The Astrophysical Journal Letters* 682, pp. L5–L8. DOI: 10.1086/590248. arXiv: 0802.3216 (cit. on pp. 9, 16).

Spitkovsky, A. and Arons, J. (2002). “Simulations of Pulsar Wind Formation”. In: *Neutron Stars in Supernova Remnants*. Ed. by P. O. Slane and B. M. Gaensler. Vol. 271. Astronomical Society of the Pacific Conference Series, p. 81. eprint: arXiv:astro-ph/0201360 (cit. on p. 4).

Tanaka, S. J. and Takahara, F. (June 2010). “A Model of the Spectral Evolution of Pulsar Wind Nebulae”. In: *The Astrophysical Journal* 715, pp. 1248–1257. DOI: 10.1088/0004-637X/715/2/1248. arXiv: 1004.3098 [astro-ph.HE] (cit. on p. 21).

– (Nov. 2011). “Study of Four Young TeV Pulsar Wind Nebulae with a Spectral Evolution Model”. In: *The Astrophysical Journal* 741, 40, p. 40. DOI: 10.1088/0004-637X/741/1/40. arXiv: 1108.1690 [astro-ph.HE] (cit. on p. 21).

Willmann, Philipp (2012). “Spatially Resolved X-Ray Spectroscopy and Modeling of the Non-Thermal Emission of the Pulsar Wind Nebula in G21.5–0.9”. Diploma Thesis. Friedrich-Alexander-Universittät Erlangen-Nürnberg (cit. on pp. 5, 19, 21).

Wilms, J., Allen, A., and McCray, R. (Oct. 2000). “On the Absorption of X-Rays in the Interstellar Medium”. In: *The Astrophysical Journal* 542, pp. 914–924. DOI: 10.1086/317016. eprint: arXiv:astro-ph/0008425 (cit. on p. 14).

Yatsu, Y., Kawai, N., Shibata, S., and Brinkmann, W. (Feb. 2009). “Discovery of the Inner Ring around PSR B1509-58”. In: *Publications of the Astronomical Society of Japan* 61, pp. 129–. arXiv: 0808.0581 (cit. on pp. 5, 19, 21).

A. X-ray Data

Table 8: X-Ray input data for the model in erg/cm^2/s, resolved into the 6 annuli and 5 energy bins after combining bins 5 and 6

	annulus 1	annulus 2
combined flux	$1.303 \cdot 10^{-11} \pm 2.039 \cdot 10^{-13}$	$1.338 \cdot 10^{-11} \pm 3.513 \cdot 10^{-13}$
flux bin 1	$4.661 \cdot 10^{-12} \pm 1.381 \cdot 10^{-13}$	$5.414 \cdot 10^{-12} \pm 2.539 \cdot 10^{-13}$
flux bin 2	$2.476 \cdot 10^{-12} \pm 7.154 \cdot 10^{-14}$	$2.603 \cdot 10^{-12} \pm 1.263 \cdot 10^{-13}$
flux bin 3	$1.984 \cdot 10^{-12} \pm 7.775 \cdot 10^{-14}$	$2.021 \cdot 10^{-12} \pm 1.349 \cdot 10^{-13}$
flux bin 4	$1.541 \cdot 10^{-12} \pm 8.222 \cdot 10^{-14}$	$1.312 \cdot 10^{-12} \pm 1.330 \cdot 10^{-13}$
flux bin 5*	$2.289 \cdot 10^{-12} \pm 1.750 \cdot 10^{-13}$	$2.089 \cdot 10^{-12} \pm 2.794 \cdot 10^{-13}$

	annulus 3	annulus 4
combined flux	$3.122 \cdot 10^{-11} \pm 5.374 \cdot 10^{-13}$	$3.349 \cdot 10^{-11} \pm 6.099 \cdot 10^{-13}$
flux bin 1	$1.395 \cdot 10^{-11} \pm 3.934 \cdot 10^{-13}$	$1.583 \cdot 10^{-11} \pm 4.776 \cdot 10^{-13}$
flux bin 2	$6.029 \cdot 10^{-12} \pm 1.964 \cdot 10^{-13}$	$6.165 \cdot 10^{-12} \pm 2.081 \cdot 10^{-13}$
flux bin 3	$4.229 \cdot 10^{-12} \pm 1.947 \cdot 10^{-13}$	$4.387 \cdot 10^{-12} \pm 2.173 \cdot 10^{-13}$
flux bin 4	$2.882 \cdot 10^{-12} \pm 2.081 \cdot 10^{-13}$	$2.747 \cdot 10^{-12} \pm 2.204 \cdot 10^{-13}$
flux bin 5*	$3.729 \cdot 10^{-12} \pm 4.435 \cdot 10^{-13}$	$3.140 \cdot 10^{-12} \pm 4.996 \cdot 10^{-13}$

	annulus 5	annulus 6
combined flux	$2.807 \cdot 10^{-11} \pm 6.240 \cdot 10^{-13}$	$1.973 \cdot 10^{-11} \pm 9.307 \cdot 10^{-13}$
flux bin 1	$1.511 \cdot 10^{-11} \pm 4.834 \cdot 10^{-13}$	$1.302 \cdot 10^{-11} \pm 5.158 \cdot 10^{-13}$
flux bin 2	$5.133 \cdot 10^{-12} \pm 2.136 \cdot 10^{-13}$	$3.554 \cdot 10^{-12} \pm 2.614 \cdot 10^{-13}$
flux bin 3	$3.773 \cdot 10^{-12} \pm 2.310 \cdot 10^{-13}$	$2.949 \cdot 10^{-12} \pm 2.420 \cdot 10^{-13}$
flux bin 4	$2.270 \cdot 10^{-12} \pm 2.388 \cdot 10^{-13}$	$1.861 \cdot 10^{-12} \pm 2.653 \cdot 10^{-13}$
flux bin 5*	$2.929 \cdot 10^{-12} \pm 6.085 \cdot 10^{-13}$	$2.307 \cdot 10^{-12} \pm 5.328 \cdot 10^{-12}$

Erklärung

Hiermit bestätige ich, dass ich diese Arbeit selbstständig und nur unter Verwendung der angegebenen Hilfsmittel angefertigt habe.

Erlangen, den 30.06.2013

Sebastian Meßlinger